TITLE:

Friction of Polymer Chains under Fast Deformation(Dissertation_全文)

AUTHOR(S):

Yaoita, Takatoshi

CITATION:

Yaoita, Takatoshi. Friction of Polymer Chains under Fast Deformation. 京都大学, 2014, 博士(工学)

ISSUE DATE:

2014-11-25

URL:

https://doi.org/10.14989/doctor.k18656

RIGHT:

京都大学学術情報リポジトリ
KURENAI 紅
Kyoto University Research Information Repository

Friction of Polymer Chains under Fast Deformation

Takatoshi Yaoita

2014

Contents

CHAPTER 3

Uniaxial elongational viscoelastic behavior investigated through a multi-chain model

CHAPTER 4

Uniaxial elongational viscoelastic behavior investigated through a single-chain model

CHAPTER 5

Nonlinear stress relaxation in coarse-grained molecular dynamics simulations

CHAPTER 6

List of Publications

CHAPTER 1
Introduction

1-1. Background

Under flow, flexible polymeric liquids exhibit viscoelastic responses that reflect the polymer chain motion in the flow field. When the flow is slower than the equilibrium chain motion, the viscoelastic response reflects the equilibrium dynamics and thus becomes linear to the flow rate. In contrast, the polymer chain exhibits non-equilibrium dynamics and the corresponding nonlinear responses under fast flow.[1)-6)] This non-equilibrium dynamics is of scientific as well as industrial interest, the latter being intimately related to fiber-spinning,[7)] film-stretching,[8)] and so on. The non-equilibrium dynamics is usually accompanied by highly stretched/oriented conformation of polymer chains far from the Gaussian conformation at equilibrium.

Such non-equilibrium dynamics under fast flow has been subjected to extensive researches from both experimental and theoretical points of view,[1)-6)] but no full understanding has been established. A brief summary of the results of those researches is given below, firstly for the experimental researches and then for the theoretical researches.

1-2. Characteristic features deduced from experimental data

It has been established that linear viscoelastic responses of polymers are universal, if the ratio of the molecular weight to a certain characteristic value is the same. An example of such universality (master response function) of linear viscoelasticity of entangled polymers is shown in Fig. 1-1. Figure 1-1 shows the data for melts of different chemistries, *i.e.*, polystyrene (PS)[9] and polyisoprene (PI).[10] The figure also shows the data for different concentrations of PS solutions.[9] The data for each liquid were made owing to the time-temperature superposition principle. In the plot, the effects of experimental conditions were embedded in the plateau modulus G_N^0 and the longest relaxation time τ_1 which are used to reduce the storage and loss moduli, G' and G'', and the angular frequency, ω, respectively. (The reduced quantities are indicated with tilde on top.) The molecular weights are chosen as indicated in the Figure caption to attain a similar number of entanglement segments per molecule, $Z \cong 20$. This Z value is the ratio of the molecular weight of the polymer M to the entanglement molecular weight M_e, the latter being related to G_N^0 as $M_e = \rho RT / G_N^0$ (Here ρ is the density of the liquid). Figure 1-1 clearly shows that the universality is observed in a wide range of frequency from the Rouse relaxation (in high frequency) to the terminal flow region (in low frequency) through the rubbery plateau region.

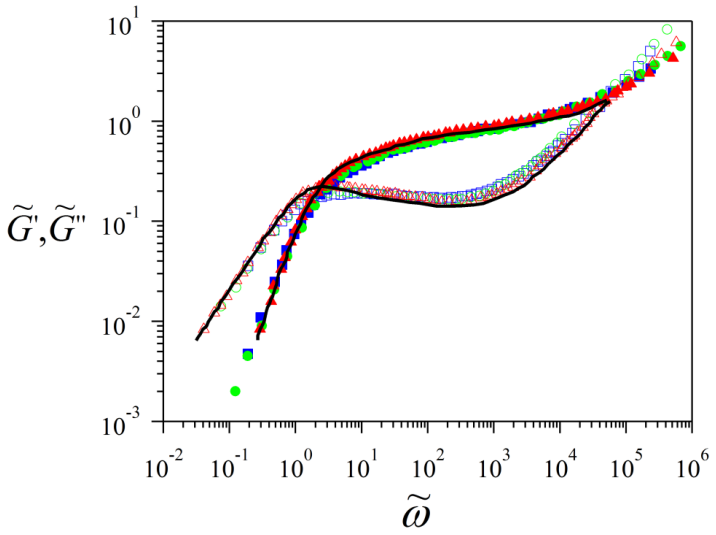

Figure 1-1 Reduced storage $\widetilde{G}'$(filled symbols) and loss $\widetilde{G}''$ (unfilled symbols) moduli for several monodisperse polymer liquids as functions of reduced frequency $\widetilde{\omega}$. Storage (G') and loss (G'') moduli for 52wt% PS solution (■ and □; weight-average molecular weight M_w = 5.5x10^2 kg/mol) at 343 K,[9] PS melt (● and ○; M_w = 2.9x10^2 kg/mol) at 403K,[9] and PI melt (▲ and △; M_w = 95 kg/mol) at 298 K,[10] respectively, are reduced to G'/G_N^0 and G''/G_N^0 by plateau modulus (G_N^0) in vertical axis. These reduced moduli are plotted against the angular frequency reduced by longest relaxation time (τ_1), $\omega\tau_1$. G_N^0 and τ_1 adopted for the plot are 6.2x10^4 Pa and 2.4 s for the PS solution,[9] 2.5x10^5 Pa and 6.8x10^3 s for the PS melt,[9] and 4.8x10^5 Pa[10] and 0.23 s for the PI melt, respectively. The samples have similar number of entanglement per chain (Z) estimated as 21 for the PS solution,[9] 21 for the PS melt,[9] and 20 for the PI melt,[10] respectively. Curves indicate predictions[9] for the PI melt by the Likhtman-McLeish model.[36]

Similar universality for solutions and melts has been reported under fast shear flows if the shear rate reduced with respect to the longest relaxation time, $\widetilde{\dot{\gamma}} = \dot{\gamma}\tau_1$, is identical and their Z values are similar to each other. An example of the universal plot is shown in Fig. 1-2 where the reduced transient shear viscosity growth function, $\widetilde{\eta}_S^+ \equiv \eta_S^+ / G_N^0\tau_1$, is plotted against a reduced time, $\widetilde{t} = t/\tau_1$. The data shown in Fig. 1-2 includes those for a PS melt[11] and a PS solution,[12] PI melt,[10] and polybutadiene (PB) solution.[13] The universality is observed for a pair of the data set for the PS melt (Z =13) and the PS solution (Z =15), and for another pair of the data set for the PI melt (Z =20) and the PB

solution (Z =19). For $\tilde{\dot{\gamma}} < 1$, the viscoelastic response is linear so that the universality in linear viscoelasticity (shown in Fig. 1-1) guarantees the universality of $\tilde{\eta}_S^+$ by construction. Such a data set is omitted here for clarity, and all the data shown here are obtained at $\tilde{\dot{\gamma}} > 1$ where $\tilde{\eta}_S^+$ shows nonlinearity. Figure 1-2 shows that $\tilde{\eta}_S^+$ is universal, including the overshoot behavior, even under such fast flow if comparison is made for the pair with similar Z and $\tilde{\dot{\gamma}}$ values. Consequently, the steady state viscosity η_S becomes also universal if η_S is reduced to $\tilde{\eta}_S \left(\equiv \eta_S / G_N^0 \tau_1 \right)$ and plotted against $\tilde{\dot{\gamma}}$ for similarly entangled liquids as shown in Fig. 1-3.

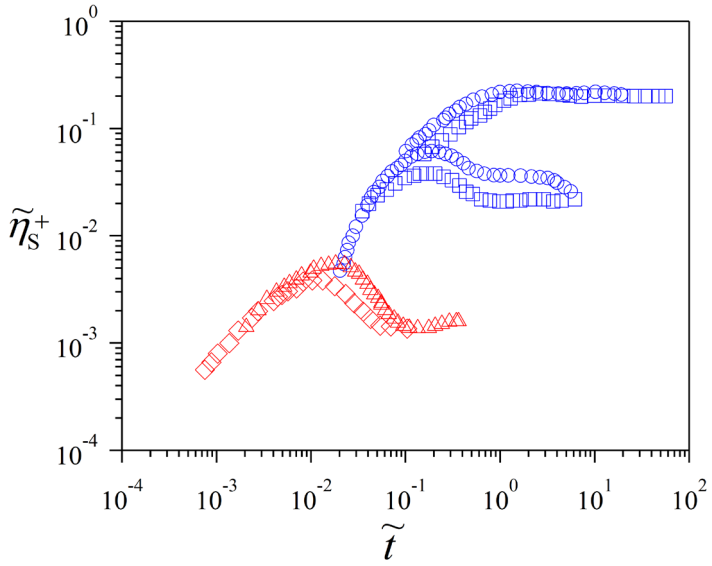

Figure 1-2 Reduced shear viscosity growth functions ($\tilde{\eta}_S^+$) for several polymer liquids. Viscosity growth functions (η_S^+) for 5wt% PS solution (□; weight-average molecular weight M_w = 5.5x10^3 kg/mol) at 273 K,[12] PS melt (○; M_w = 2.0x10^2 kg/mol) at 448 K,[11] and PI melt (△; M_w = 95 kg/mol) at 238 K[10] and 7wt% PB solution (◇; M_w = 8.1x10^2 kg/mol) at 298 K[13] are reduced to $\eta_S^+ / G_N^0 \tau_d$. This reduced viscosity growth function is plotted against a time t / τ_1 reduced by longest relaxation time (τ_1). G_N^0 and τ_1 adopted for the reduced plot are 210 Pa and 144 s for the PS solution, 2.5x10^5 Pa and 1.33 s for the PS melt, 4.8x10^5 Pa and 700 s for the PI melt, and 5.2x10^4 Pa and 86 s for the PB solution, respectively. The number of entanglement per chain (Z) is 13, 15, 20, and 19 for the PS solution, the PS melt, the PI melt, and the PB solution, respectively. Reduced strain rate $\tilde{\dot{\gamma}} \left(\equiv \dot{\gamma} \tau_1 \right)$ are 1.6 and 19 for the PS solution, 1.3 and 13 for the PS melt, and 250 for the PI melt and 230 for the PB solution, respectively.

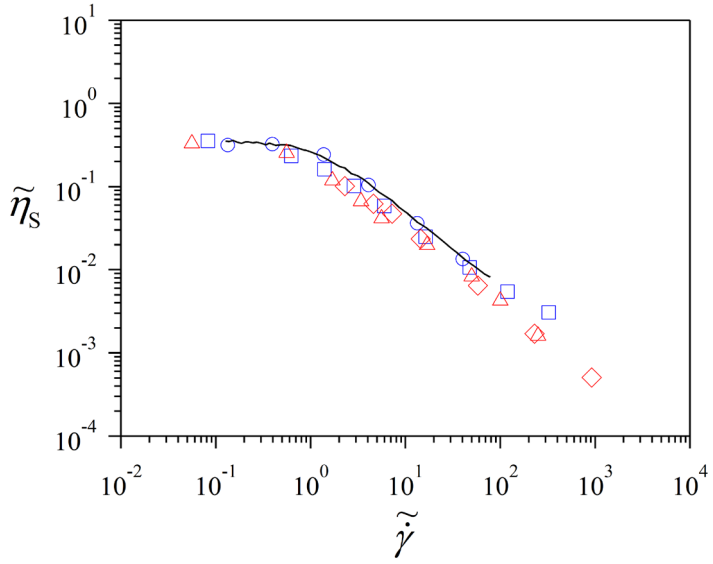

Figure 1-3 Reduced steady state shear viscosities ($\tilde{\eta}_S$) for the samples in Fig. 1-2. Steady state viscosity (η_S) for the PS solution (□; $Z = 13$),[12] the PS melt (○; $Z = 15$),[11] and the PI melt (△; $Z = 20$),[10] and the PB solution (◇; $Z = 19$)[13] are reduced to $\eta_S / G_N^0 \tau_1$ and plotted against the reduced shear rate, $\tilde{\dot{\gamma}} = \dot{\gamma}\tau_1$. Curve is the prediction[11] for the PS melt by the Mead-Larson-Doi model.[41]

Despite the universality mentioned above, experiments also indicate that the universality vanishes for uniaxial elongational viscosity.[9),14)-20)] Figure 1-4 shows the reduced transient uniaxial elongational viscosity growth function, $\tilde{\eta}_E^+(\tilde{t}, \tilde{\dot{\varepsilon}})$, for a pair of similarly entangled PS solution[15] and melt[17] at several reduced elongational strain rates $\tilde{\dot{\varepsilon}} (\equiv \dot{\varepsilon}\tau_1)$. As similar to the behavior of shear viscosity growth function, $\tilde{\eta}_S^+$ (Fig. 1-2), the universality of $\tilde{\eta}_E^+$ for solution and melt is observed even at $\tilde{\dot{\varepsilon}} > 1$ given that $\tilde{\dot{\varepsilon}}$ is lower than a certain critical value; For instance, $\tilde{\eta}_E^+$ of the solution at $\tilde{\dot{\varepsilon}} = 60$ is similar to of the melt at $\tilde{\dot{\varepsilon}} = 34$. On the other hand, at higher $\tilde{\dot{\varepsilon}}$, the universality vanishes and $\tilde{\eta}_E^+$ becomes concentration dependent; In Fig. 1-4, $\tilde{\eta}_E^+$ for the solution at $\tilde{\dot{\varepsilon}} = 126$ grows up to a steady state value being higher than that for the melt at $\tilde{\dot{\varepsilon}} = 113$. This lack of universality is clearly observed also in the reduced steady state uniaxial

viscosity $\tilde{\eta}_E$ shown in Fig. 1-5. $\tilde{\eta}_E$ of the PS solution[15] shows an upturn at a critical $\tilde{\dot{\varepsilon}}$, whereas $\tilde{\eta}_E$ of the PS melt[17] monotonically decreases in the whole range of $\tilde{\dot{\varepsilon}}$. Quite recently, further experimental data have been reported for similarly entangled PI solution and melt.[20] In Fig. 1-5, those data are compared with the data for PS solution and melt. The PI melt shows an upturn, which is similar to the behavior of the PS solution but quite different from the behavior of the PS melt. Consequently, $\tilde{\dot{\varepsilon}}$ dependence of $\tilde{\eta}_E$ changes with the chemistry of polymer. The data also show that the critical $\tilde{\dot{\varepsilon}}$ value for the upturn is concentration dependent in the PI liquids, being lower for the melt than for the solution. Namely, $\tilde{\eta}_E$ of the PI solution and melt exhibit different $\tilde{\dot{\varepsilon}}$ dependence of $\tilde{\eta}_E$, which makes a contrast from the universality observed for the reduced shear viscosity, $\tilde{\eta}_S$ (Fig. 1-3).

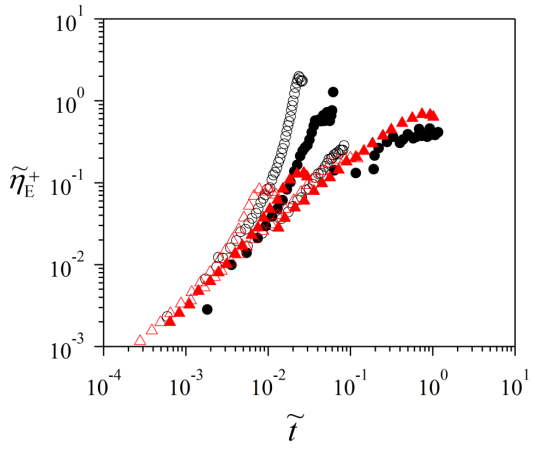

Figure 1-4 Reduced uniaxial elongational viscosity growth functions ($\tilde{\eta}_E^+$) for PS solution and melt. $\tilde{\eta}_E^+$ for 10wt% solution (symbols in black; M_w = 3.9x10^3 kg/mol) at 294 K[15] and melt (symbols in red; M_w = 3.9x10^2 kg/mol) at 403 K[17] are reduced to $\eta_E^+ / G_N^0 \tau_d$ and plotted against a reduced time, $\tilde{t} = t / \tau_1$. The samples have similar number of entanglement per chain, $Z \cong 27$ and 29 for the solution and the melt, respectively G_N^0 and τ_1 are 1360 Pa and 17.2 s for the solution,[15] and 2.0x10^5 Pa and 11351 s for the melt.[19] The reduced strain rates $\tilde{\dot{\varepsilon}} (\equiv \dot{\varepsilon}\tau_1)$ are 1.7, 60, 126, and 201 for the solution, and 3.4, 34, 113, and 340 for the melt, both from right to left.

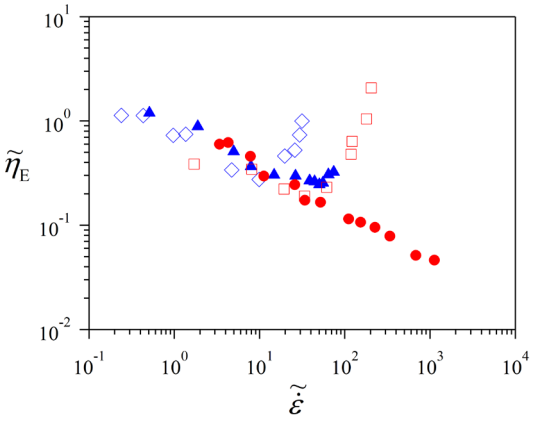

Figure 1-5 Reduced steady state uniaxial elongational viscosity ($\tilde{\eta}_E$) for PS and PI solution/melt as a function of reduced strain rate ($\tilde{\dot{\varepsilon}}$). Steady state uniaxial viscosities (η_E) for the 10wt% PS solution (□; M_w = 3.9x10^3 kg/mol) at 294 K,[15] the PS melt (●; M_w = 3.9x10^2 kg/mol) at 403 K,[17] the 14wt% PI solution (◇; M_w = 1.1x10^3 kg/mol) at 295 K,[20] and the PI melt (▲; M_w = 1.5x10^2 kg/mol) at 295 K[20] are reduced to $\eta_E / G_N^0 \tau_d$ and plotted against the reduced strain rate, $\tilde{\dot{\varepsilon}} = \dot{\varepsilon}\tau_1$. The data of the PS solution/melt are the same set in Fig. 1-4. G_N^0 and τ_1 are 6.4x10^3 Pa and 0.43 s for the PI solution, and 3.5x10^5 Pa and 0.43 s for the PI melt. The samples have similar number of entanglement per chain, $Z \cong$ 27, 29, 28, and 29 for the PS solution, PS melt, PI solution, and PI melt, respectively.

1-3. Theoretical models

The universality in the viscoelastic responses has encouraged the development of generic models for polymer dynamics. Such models are constructed on the basis of the coarse-graining idea, in which the degrees of freedom (*i.e.*, position and momentum of each atom) are reduced to fewer state valuables.[4),21)] This manipulation smears the chemistry details of the molecule and casts their effects into a few parameters for the chosen state valuables. For the case of polymers, the center-of-mass of several repeating units and its momentum are chosen as the coarse-grained state valuables. The chosen group of the repeating units is referred to as segment, and consecutive segments represent a polymer chain. Molecular models in such a coarse-grained level have been developed. Some examples of the models are summarized below, first for non-entangled polymers and then for entangled polymers.

1-3-1. Rouse model for non-entangled polymers

The most fundamental coarse-grained model for polymer dynamics is the Rouse model[21)] (Fig. 1-6), in which a chain is subdivided into N segments each having an average length b at equilibrium. No specific interaction between segments is considered.

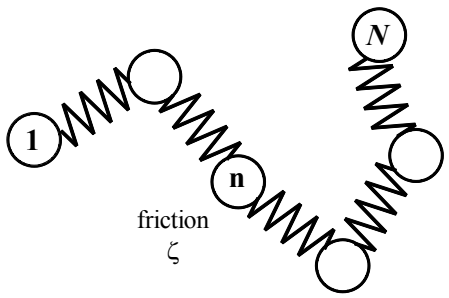

Figure 1-6 Rouse model[21)]

In the Rouse model, the motion of the segment is described by the Langevin equation,

$$\mathbf{F}_{\mathrm{el},n} + \mathbf{F}_{\mathrm{drag},n} + \mathbf{F}_{\mathrm{rand},n} = 0 \qquad (1.1).$$

The first term in LHS is the elastic force acting on n-th segment due to the neighbor segments connected thereto. This force is determined by the positions of n-th segment $\mathbf{R}_n$ and its neighbor segments as

$$\mathbf{F}_{\mathrm{el},n} = -\kappa[2\mathbf{R}_n - \mathbf{R}_{n+1} - \mathbf{R}_{n-1}] \quad \text{for inner segments } (n = 2, 3, .., N\text{-}1) \qquad (1.2b),$$

$$\mathbf{F}_{\mathrm{el},1} = -\kappa[\mathbf{R}_1 - \mathbf{R}_2],\ \mathbf{F}_{\mathrm{el},N} = -\kappa[\mathbf{R}_N - \mathbf{R}_{N-1}] \quad \text{for end segments} \qquad (1.2b),$$

κ is the spring constant that is expressed in terms of the segment length b, Boltzman constant k_{B}, and absolute temperature T as

$$\kappa = \frac{3k_{\mathrm{B}}T}{b^2} \qquad (1.3).$$

This expression of κ is derived from the Gaussian chain assumption for the repeating units involved in the segment.

The second and the third terms in LHS of Eq. 1.1 indicate the stochastic forces that replace collisions among atoms. With the Markov approximation[22] (that assumes the inter-atomic collisions to be homogeneous, isotropic, and non-correlated), the stochastic forces can be characterized by a scalar quantity called friction coefficient ζ. The drag force is expressed in terms of this ζ and the flow velocity at the position of n-th segment, $\mathbf{V}(\mathbf{R}_n)$, as

$$\mathbf{F}_{\mathrm{drag},n} = -\zeta\left[\frac{d\mathbf{R}_n}{dt} - \mathbf{V}(\mathbf{R}_n)\right] \qquad (1.4a).$$

For the shear and extensional flow fields, $\mathbf{V}(\mathbf{R}_n)$ can be expressed as

$$\text{shear}: \mathbf{V}(\mathbf{R}_n) = \begin{bmatrix} \dot{\gamma}R_{n,y} \\ 0 \\ 0 \end{bmatrix} \qquad (1.4b),$$

$$\text{extensional}: \mathbf{V}(\mathbf{R}_n) = \begin{bmatrix} -\dot{\varepsilon} R_{n,x}/2 \\ -\dot{\varepsilon} R_{n,y}/2 \\ \dot{\varepsilon} R_{n,z} \end{bmatrix} \tag{1.4c},$$

where $R_{n,\xi}$ indicates the ξ-component of $\mathbf{R}_n$ ($\xi = x, y, z$). The random force $\mathbf{F}_{\text{rand}}$ should be commensurate with this drag force and should have the Gaussian, white noise feature characterized by[23)]

$$< \mathbf{F}_{\text{rand},n}(t) >= 0 \quad \text{and} \quad < \mathbf{F}_{\text{rand},n}(t)\mathbf{F}_{\text{rand},m}(t') >= 2\zeta k_{\text{B}} T \delta_{mn} \delta(t-t')\mathbf{I} \tag{1.5},$$

where δ_{nm}, $\delta(t)$, and $\mathbf{I}$ indicate the Kronecker delta, delta function of t, and unit tensor, respectively. The stress tensor ($\boldsymbol{\sigma}$) is calculated by Kramers expression[24),25)] owing to the stress-optical rule;[26)]

$$\boldsymbol{\sigma}(t) = 3\nu k_{\text{B}} T \mathbf{S}(t) \quad \text{with} \qquad \mathbf{S}(t) = \frac{1}{b^2} \sum_{n=1}^{N-1} < \mathbf{u}_n(t)\mathbf{u}_n(t) > \tag{1.6}.$$

Here, ν is the number density of the chains, and $\mathbf{S}(t)$ is the orientation tensor defined with respect to the bond vector between n-th and (n+1)-th segment, $\mathbf{u}_n(t) = \mathbf{R}_{n+1}(t) - \mathbf{R}_n(t)$.

Equations 1.1 and 1.6 can be cast into non-dimensional form when the variables therein are reduced by respective units (for example, $\mathbf{R}_n(t)$ and $\mathbf{u}_n(t)$ are reduced by the segment size b). Thus, the Rouse model suggests that response functions are universal, if the measured quantities are reduced in this way. This universality is summarized below for representative flow fields.

For an infinitesimal step shear strain γ_0 (in the linear viscoelastic regime) applied on the x-z plane in the x direction, the shear rate appearing in Eq. 1.4b is expressed as $\dot{\gamma}(t) = \gamma_0 \delta(t)$. For this $\dot{\gamma}(t)$, the relaxation modulus $G(t)$ (= $\sigma_{xy}(t)/\gamma_0$) can be easily

calculated from Eqs. 1.1-1.6 with the continuous limit approximation. The result is summarized as

$$\frac{G(t)}{\nu k_{\mathrm{B}}T}=\sum_{p=1}^{N-1}\exp\left(-p^2\frac{t}{\tau_1}\right)\qquad\text{with}\qquad\tau_1=\frac{\zeta b^2N^2}{6\pi^2k_{\mathrm{B}}T}\tag{1.7}$$

Namely, the reduced moduli $G(t)/\nu k_{\mathrm{B}}T$ of different systems (*e.g.*, solutions and melts) calculated from the Rouse model are universally dependent on the reduced time t/τ_1, given that the segment number per chain, N, is common for those systems.

After start up of shear flow at a rate $\dot{\gamma}$, Equations 1.1-1.6 give the shear viscosity growth function, $\eta_{\mathrm{S}}^{+}(t)$, that can be cast in a reduced form,

$$\frac{\eta_{\mathrm{S}}^{+}(t)}{\nu k_{\mathrm{B}}T\tau_1}=\sum_{p=1}^{N-1}\frac{1}{p^2}\left[1-\exp\left(-p^2\frac{t}{\tau_1}\right)\right]\tag{1.8}$$

This reduced function, $\eta_{\mathrm{S}}^{+}(t)/\nu k_{\mathrm{B}}T\tau_1$, being universally dependent on the reduced time t/τ_1 for systems having the common N, is independent of $\dot{\gamma}$. Namely, the Rouse model exhibits no nonlinearity in the shear stress even under fast shear at $\dot{\gamma}>1/\tau_1$.

The situation is different under the elongation flow specified by Eq. 1.4c. The elongational viscosity growth function η_{E}^{+}, calculated from Eqs. 1.1-1.6, can be cast in the reduced form,

$$\begin{aligned}\frac{\eta_{\mathrm{E}}^{+}(t/\tau_1;\tilde{\dot{\varepsilon}})}{\nu k_{\mathrm{B}}T\tau_1}=&\frac{1}{\tilde{\dot{\varepsilon}}}\sum_{p=1}^{N-1}\frac{1}{1-(2\tilde{\dot{\varepsilon}}/p^2)}\left[1-(2\tilde{\dot{\varepsilon}}/p^2)\exp\left(-(p^2-2\tilde{\dot{\varepsilon}})\frac{t}{\tau_1}\right)\right]\\&-\frac{1}{\tilde{\dot{\varepsilon}}}\sum_{p=1}^{N-1}\frac{1}{1+(\tilde{\dot{\varepsilon}}/p^2)}\left[1+(\tilde{\dot{\varepsilon}}/p^2)\exp\left(-(p^2+\tilde{\dot{\varepsilon}})\frac{t}{\tau_1}\right)\right]\end{aligned}\tag{1.9}$$

where $\tilde{\dot{\varepsilon}}=\dot{\varepsilon}\tau_1$. For $\dot{\varepsilon}\to 0$, this η_{E}^{+} coincides with $3\eta_{\mathrm{S}}^{+}(t)$ and the Trouton limit is recovered. However, for larger $\dot{\varepsilon}$, η_{E}^{+} of the Rouse model is dependent on $\dot{\varepsilon}$ and nonlinearity prevails (which is qualitatively different from the behavior of the shear viscosity growth function, $\eta_{\mathrm{S}}^{+}(t)$). In particular, η_{E}^{+} diverges as the elongational rate

$\dot{\varepsilon}$ approaches $1/2\tau_1$ (= terminal relaxation frequency for the end-to-end distance of the Rouse chain). Nevertheless, Equation 1.9 demonstrates the universality, including that for the nonlinearity and divergence, for different systems (*e.g.*, solutions and melts), given that N and the reduced elongational rate $\tilde{\dot{\varepsilon}}$ are common for those systems.

The universality deduced from the Rouse model is in harmony with the linear viscoelastic behavior of non-entangled polymers under small strain and/or shear flow at various rates, $\dot{\gamma}$. As an example, Figure 1-7 demonstrates that the Rouse prediction (solid curves) is favorably compared with the linear viscoelastic moduli data of barely entangled PS melt (M_w = 28.9 kg/mol; symbols).[27] (The elongational behavior of non-entangled polymers has been much less extensively studied, as compared to the shear behavior. However, studies of dilute solutions suggested qualitative agreement of Eq. 1.9 with the data.)

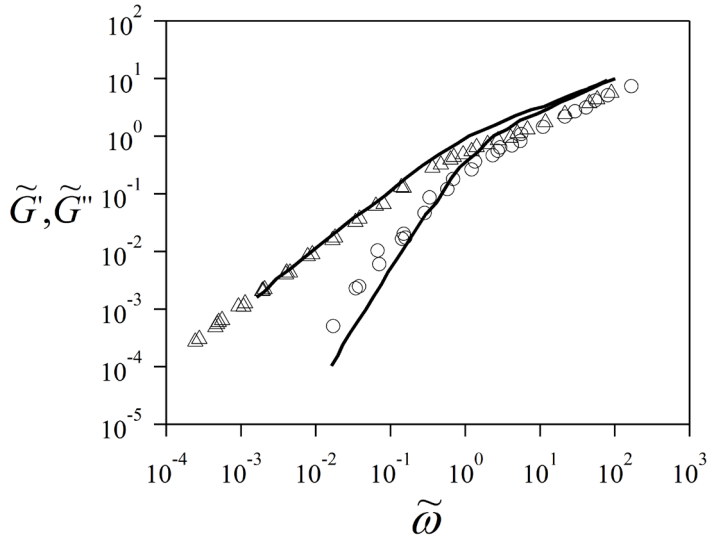

Figure 1-7 Reduced storage (○) and loss (△) moduli plotted against reduced frequency for PS melt with M_w = 28.9 kg/mol at 433 K.[27] $\nu k_B T$ and τ_1 adopted are 1.3×10^5 Pa and 4×10^{-2} s, respectively. The Rouse prediction is drawn with the solid curves.

1-3-2. Tube model for entangled polymers and its problem

The success of the Rouse model has encouraged further development of the model(s) for entangled polymers that exhibit prominent viscoelastic behavior. A rigorous approach is based on the projection operator technique[22] that derives the stochastic forces in the Langevin equation deductively from the smeared fast dynamics. A few papers reported success of this approach, but the success was achieved only for linear viscoelastic behavior.[28-30] Instead of the deductive approach, inductive approach of modeling the entangled polymer dynamics has been attempted extensively to achieve remarkable success.

The most successful example of inductive modeling of entangled polymer dynamics is the tube model that was proposed by Edwards[31] and de Gennes[2] and was further developed by Doi and Edwards (DE).[4] The tube model reduces the entangled polymer dynamics to a motion of a Rouse chain confined in a tube (*cf*. Fig. 1-8). The tube represents topological constraints from the surrounding chains. The Rouse chain freely diffuses with a certain friction along the tube but its lateral motion is constrained within the tube diameter. Thus, in the classical tube model, the segment size of the Rouse chain in the tube is taken to be identical to the tube diameter a, a material parameter characterizing the entanglement density, and the local/fast dynamics below this length scale is smeared out. Such Rouse segment is called entanglement segment. The stress tensor in the tube model is obtained from the Kramers expression (Eq. 1.6).

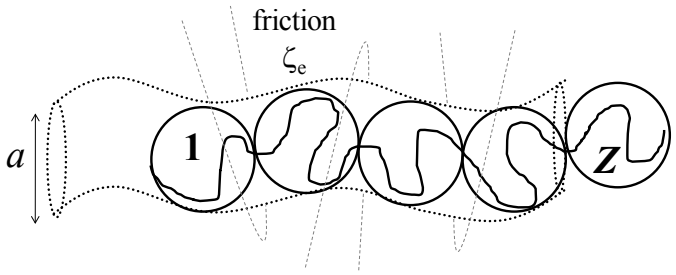

Figure 1-8 Tube model[4)]

As similar to the Rouse model, the tube model suggests universality for polymer dynamics and viscoelasticity. Namely, the equation of motion of the entanglement segment can be cast in a non-dimensional form when the variables therein are reduced by respective units, *i.e.*, the unit length a, the unit energy k_BT, and the unit time $\tau_e = \zeta_e a^2 / 3\pi^2 k_B T$ (where ζ_e is the friction coefficient of the entanglement segment). The chain molecular weight is reduced by the molecular weight M_e of the entanglement segment to give the number of entanglement per chain, Z. Correspondingly, the viscoelastic responses deduced from the tube model exhibit the universality, as explained below in more detail.

The classical tube model assumes that the tube is fixed in space and the Rouse chain therein exhibits no fluctuation of its length measured along the tube. For this case, the chain relaxes only through the cooperative curvilinear diffusion referred to as "reptation", and the corresponding relaxation modulus $G(t)$ in the linear viscoelastic regime is expressed as[4)]

$$\frac{G(t)}{G_N^0} = P(t) = \sum_{p\,odd} \frac{8}{\pi^2 p^2} \exp\left(- p^2 \frac{t}{\tau_1} \right) \qquad (1.10),$$

with

$$\tau_1 = \frac{\zeta_e a^2}{\pi^2 k_B T} Z^3 = 3Z^3 \tau_e \quad \text{(longest reptation time)} \tag{1.11}.$$

In a given time scale t, a "surviving" portion of the initial tube has not been visited by the chain end, and this portion preserves the initial orientational anisotropy (that is equivalent to the initial stress; *cf*. Eq. 1.6). The remaining portion has been visited by the chain end and loses its initial anisotropy. $P(t)$ appearing in Eq. 1.10 is the tube survival probability that is defined as a ratio of the length of the surviving portion to the whole length of the initial tube. Equations 1.10 and 1.11 clearly indicate that the reduced relaxation modulus $G(t)/G_N^0$ of different systems (*e.g.*, solutions and melts) is universally dependent on the reduced time, t/τ_1.

The universality of the linear viscoelastic response thus deduced from the classical tube model is qualitatively consistent with that observed for entangled linear polymers having different concentrations and/or different chemical structure. However, the predicted $G(t)$ (Eqs. 1.10 and 1.11) is not in quantitative agreement with experiments; for example, the predicted τ_1 and relaxation mode distribution are much larger and narrower, respectively, than the experimental data.[32] Thus, the tube model has been refined through incorporation of additional molecular mechanisms competing with reptation. These additional mechanisms include the contour length fluctuation (CLF)[4] due to the spring-like motion of the Rouse chain in the tube and the constraint release (CR)[33-35] implementing the tube motion due to the motion of the surrounding (tube-forming) chains. Some of the smeared fast dynamics are added as Rouse modes as well to reproduce the short time responses. Modern tube theories that implement these mechanisms can describe the linear viscoelastic data quantitatively. For example, Figure

1-1 demonstrates good agreement of the reduced storage and loss moduli predicted by the Likhtman-McLeish (LM)[36] model, one of the modern tube models.

The tube model has been extended to nonlinear viscoelastic responses and has achieved success to reproduce the universality also in the nonlinear regime. For example, the expressions of $\eta_{\mathrm{S}}^{+}(t,\dot{\gamma})$ and $\eta_{\mathrm{E}}^{+}(t,\dot{\varepsilon})$ deduced from the classical Doi-Edwards model are cast in a form,[37]

$$\frac{\eta_{\mathrm{S}}^{+}(t,\dot{\gamma})}{G_N^0\tau_1}=\frac{1}{\tilde{\dot{\gamma}}}\int_{-\infty}^{t}dt'P(t-t')F_{\mathrm{S}}[\tilde{\dot{\gamma}}(t-t')/\tau_1] \tag{1.12a},$$

with

$$F_{\mathrm{S}}(\gamma)=\frac{1}{2\gamma}\int_0^1 dx[1+\frac{\gamma^2x^2-1}{\sqrt{x^4(\gamma^4+4\gamma^2)-2\gamma^2x^2+1}}] \tag{1.12b},$$

and

$$\frac{\eta_{\mathrm{E}}^{+}(t,\dot{\varepsilon})}{G_N^0\tau_1}=\frac{1}{\tilde{\dot{\varepsilon}}}\int_{-\infty}^{t}dt'P(t-t')F_{\mathrm{E}}[\exp[\tilde{\dot{\varepsilon}}(t-t')/\tau_1]] \tag{1.13a},$$

with

$$F_{\mathrm{E}}(\varepsilon)=\frac{3}{2}\frac{\varepsilon^3}{\varepsilon^3-1}(1-\frac{\tan^{-1}\sqrt{\varepsilon^3-1}}{\sqrt{\varepsilon^3-1}})-\frac{1}{2} \tag{1.13b},$$

where $\tilde{\dot{\gamma}}=\dot{\gamma}\tau_1$ and $\tilde{\dot{\varepsilon}}=\dot{\varepsilon}\tau_1$ are the reduced shear and elongational rates, respectively, and $P(t)$ is the tube survival probability given by Eq. 1.10. This P is fully described as a function of the reduced time t/τ_1, whereas F_{S} and F_{E} (Eqs. 1.12b and 1.13b) are solely dependent on γ and ε, *i.e.*, on the flow geometry. Thus, $\eta_{\mathrm{S}}^{+}(t,\dot{\gamma})$ and $\eta_{\mathrm{E}}^{+}(t,\dot{\varepsilon})$ deduced from the classical Doi-Edwards model exhibit the universality; namely, the model predicts that reduced $\eta_{\mathrm{S}}^{+}/G_N^0\tau_1$ and $\eta_{\mathrm{E}}^{+}/G_N^0\tau_1$ of various systems are universally dependent on t/τ_1 given that the $\tilde{\dot{\gamma}}$ and/or $\tilde{\dot{\varepsilon}}$ value is common in those systems.

For quantitative prediction of experiments under fast flow, the other molecular mechanisms, *i.e.*, chain stretching[38] and convective constraint release (CCR)[39,40] have been considered in addition to CLF and CR. Mead-Larson-Doi (MLD)[41] model is one of such modern tube models that implement these mechanisms. (Details of the MLD model are given in Chapter 4.) Figure 1-3 demonstrates that the MLD model well describes the $\widetilde{\eta}_S$ data under steady shear.

The modern tube models considering the above additional mechanisms predict universality also for the elongational flow behavior. For example, η_E deduced from those models exhibit rather sharp upturn as $\dot{\varepsilon}$ approaches the length fluctuation frequency ω_R (= Rouse relaxation frequency; $\omega_R = 1/2\tau_1$ with τ_1 being given by Eq. 1.7.) If the chain is assumed to preserve its Gaussian feature even under high elongation, the tube model prediction for this upturn is very similar to the divergence of η_E explained for the Rouse model (*cf*. Eq. 1.9). In contrast, if the hardening of highly elongated chain is incorporated in the tube model calculation, the upturn stops at a finite level of η_E. For both cases, the upturn is universal for different systems, *e.g*., for solutions and melts, given that a reduced elongational rate defined with respect to the length fluctuation frequency, $\widetilde{\dot{\varepsilon}}_R = \dot{\varepsilon}/\omega_R$, is the same in those systems. However, experiments clearly indicate that the elongational flow behavior does not exhibit such universality; *cf*. Figs. 1-4 and 1-5.

Concerning this problem of the elongational flow behavior, Leygue *et al.*[42] reported that the results both for the solution and melt can be qualitatively captured by the tube model if the maximum stretch ratio (determining the hardening of the highly elongated chain) is tuned as a fitting parameter. However, the maximum stretch ratio needs to be unrealistically small if the melt behavior is to be reproduced by the approach of Leygue

et al. Attempts have been also made to examine the effects of possible artifacts induced by the tube framework, *i.e*., decoupling approximation, single chain approximation, and implementation of CCR. Yaoita *et al*.[43] calculated η_E by a multi-chain sliplink model that does not rely on the artificial construction of the tube framework to report semi-quantitative agreement with the solution data (with the upturn) but not with the melt data.

The above results have motivated researchers to propose new molecular mechanisms, but no satisfactory explanation has been established by now. For example, incorporation of the interchain pressure (ICP)[44] in the tube model can reproduce lack of upturn of η_E observed for PS melts. However, this reproduction requires unrealistic tuning for the relaxation time of tube diameter. More importantly, physics underlying the ICP parameters and compatibility[45] of ICP with the other established molecular mechanisms have been unknown.

The other possible mechanism leading to the lack of the universality in the elongational flow behavior is changes in the segmental friction under fast flow. According to the Markov assumption for the smeared collisions explained earlier in section 1-3-1, the friction is usually considered to be a constant independent of flow rate. This assumption works well under equilibrium but might fail under fast flow. Specifically, there are two possible molecular scenarios explained below.

One possible scenario is related to an anisotropy of the friction. Giesekus[46] derived a constitutive equation assuming an anisotropic friction of the polymer. This anisotropy is coupled to the chain conformation so that the anisotropy is enhanced under faster flow. If the friction is not coupled to the conformation and stays isotropic, the model predicts monotonic increase (thickening) of the uniaxial viscosity with increasing elongational rate.

On the other hand, this thickening is suppressed and thinning prevails if the anisotropy is strongly coupled to the chain conformation. Combination of this model calculation with the data suggests that the magnitude of frictional anisotropy may depend on the polymer concentration and chemistry thereby leading to the lack of hardening for PS melts (Figs. 1-4 and 1-5). However, the physics of this coupling is unknown, and thus, analysis relating the coupling to the other molecular mechanisms is impracticable.

Another possible scenario is related to reduction of friction of the segment. Molecular dynamics simulations for unentangled polymer melts have shown that the friction decreases[47,48] under faster shear even for non-entangled short chains. Iannirubertο *et al.*[49] suggested that the segmental friction reduction for a given chain is induced by the orientation and stretch of surrounding chains, and that the magnitude of this reduction may vary according to the polymer concentration. This important idea of segmental friction reduction has never been examined.

1-4. Scope of this thesis

Motivated by the experiments described in section 1-2 (universality of shear flow behavior and the lack of universality of elongational flow behavior) and the theoretical modeling described in section 1-3 (universality even under elongational flow deduced from conventional tube models), the author of this thesis investigates "reduction of segmental friction" under flow, the important molecular concept that has never been examined from experimental point of view. The results of investigation (from experimental as well as theoretical points of view) are summarized in this thesis. The thesis is composed of five chapters including this introduction as the first chapter.

Chapter 2 focuses on literature data for the stress relaxation of a PS melt[50] and solutions[15] after cessation of fast elongation. The change (reduction) of the segmental friction is evaluated from those data, and an empirical formula is proposed to describe the friction change as a function of the magnitude of stretch/orientation of the chain.

In Chapters 3 and 4, the empirical formula for the segmental friction obtained in Chapter 2 is incorporated in molecular models to calculate the uniaxial elongational viscosities for PS melts and solutions. The multi-chain slip-link simulation and the MLD model are utilized as the models in Chapters 3 and 4, respectively.

Chapter 5 conducts the Kremer-Grest-type[51] molecular dynamics simulation to extract the changes of the segmental friction for non-entangled chains. The result is compared with that obtained from experimental data in Chapter 2.

Finally, the conclusion of this thesis is summarized in Chapter 6.

References

1) W. W. Graessley, Advances in Polymer Science, 16, 1-179 (1974).

2) P. G. de Gennes, Journal of Chemical Physics, 55, 572 (1971).

3) J. D. Ferry, *Viscoelastic Properties of Polymers*, (Wiley, New York, 1980).

4) M. Doi, S. F. Edwards, *"The theory of polymer dynamics"*, Oxford University Press Inc, Clarendon (1986).

5) H. Watanabe, Progress in Polymer Science, 24, 1253 (1999).

6) T. C. B. McLeish, Advances in Physics, 51, 1379 (2002).

7) For example, V. B. Gupta, V. K. Kothari, *"Manufactured fibre technology"*, Chapman & Hall, London (1997).

8) For example, J. L. White, "Principles of polymer engineering rheology", Wiley-interscience (1990).

9) Q. Huang, O. Mednova, H. K. Rasmussen, N. J. Alvarez, A. L. Skov, K. Almdal, O. Hassager, Macromolecules, 46, 5026 (2013).

10) D. Auhl, J. Ramirez, A. Likhtman, P. Chambon, C. Fernyhough, Journal of Rheology, 52, 801 (2008).

11) T. Schweizer, J. van Meerveld, H. C. Öttinger, Journal of Rheology, 48, 1345 (2004).

12) T. Inoue, Y. Yamashita, K. Osaki, Macromolecules, 35, 1770 (2002).

13) E. V. Menezes, W. W. Graessley, Journal of Polymer Science : Polymer Physics Edition, 20, 1817 (1982).

14) P. K. Bhattacharjee, J. P. Oberhauser, G. H. McKinley, L. J. Leal, T. Sridhar, Macromolecules, 35, 10131 (2002).

15) P. K. Bhattacharjee, D. A. Nguyen, G. H. McKinley, T. Sridhar, Journal of Rheology,

47, 269 (2003).

16) X. Ye, R. G Larson, C. Pattamaprom, T. Sridhar, Journal of Rheology, 47, 443 (2003).

17) A. Bach, K. Almdal, H. K. Rasmussen, O. Hassager, Macromolecules, 36, 5174 (2003).

18) C. Luap, C. Muller, T. Schweizer, D. C. Venerus, Rheologica Acta, 45, 83 (2005).

19) M. H. Wagner, S. Kheirandish, O. Hassager, Journal of Rheology, 49, 1317 (2005).

20) T. Sridhar, M. Acharya, D. A. Nguyen, P. K. Bhattacharjee, Macromolecules, 47, 379 (2014).

21) P. E. Rouse, Journal of Chemical Physics, 21, 1272 (1953).

22) R. Zwanzig, Physical Review, 124, 983 (1961).

23) P. Mazur, I. Oppenheim, Physica (Amsterdam) 50, 241 (1970).

24) H. A. Kramers, Physica 11, 1 (1944).

25) R. B. Bird, C. F. Curtiss, R. C. Armstrong, O. Hassager, "*Dynamics of Polymeric Liquids, Vol. 2, Kinetic Theory*", Wiley-Interscience, New York, (1987).

26) H. Janeschitz-Kriegl, *Polymer melt rheology and flow birefringence*, (Springer, Berlin, 1983).

27) S. Onogi, T. Masuda, K. Kitagawa, Macromolecules, 3, 109 (1970).

28) G Ronca , The Journal of Chemical Physics 79, 1031 (1983).

29) W. Hess, Macromolecules 21, 2620 (1988).

30) K. S. Schweizer, M. Fuchs, G Szamel, M. Guenza and H. Tang, Macromolecular Theory and Simulations 6, 1037 (1997).

31) S. F. Edwards, Proceedings of the Physical Society, 92, 9 (1967).

32) M. Doi, S. F. Edwards, Journal of Chemical Society, Faraday Transactions II, 74, 1789 (1978).

33) W. W. Graessley, Advances in Polymer Science, 47, 67-117 (1982).

34) G Marrucci, Journal of Polymer Science : Polymer Physics Edition, 23, 159 (1985).

35) J. de Cloizeaux, Journal of Europhysics Letter, 5, 437 (1988).

36) A. E. Likhtman, T. C. B. McLeish, Macromolecules, 35, 6332 (2002).

37) M. Doi, S. F. Edwards, Journal of Chemical Society, Faraday Transactions II, 75, 38 (1979).

38) G Marrucci, N. Grizzuti, Gazzetta Chimica Italiana, 118, 179 (1988).

39) G Marrucci, Journal of Non-Newtonian Fluid Mechanics, 62, 279 (1996).

40) G Ianniruberto, G Marrucci, Journal of Non-Newtonian Fluid Mechanics, 65, 241 (1996).

41) D. W. Mead, R. G Larson, M. Doi, Macromolecules, 31, 7895 (1998).

42) A. Leygue, C. Bailly, R. Keunings, Journal of Non-Newtonian Fluid Mechanics, 136, 1 (2006).

43) T. Yaoita, T. Isaki, Y. Masubuchi, H. Watanabe, G Ianniruberto, G Marrucci, Macromolecules, 44, 9675 (2011).

44) G Marrucci, G Ianniruberto, Macromolecules, 37, 3934 (2004).

45) S. Dhole, A. Leygue, C. Bailly, R. Keunings, Journal of Non-Newtonian Fluid Mechanics, 161, 10 (2009).

46) H. Giesekus, Journal of Non-Newtonian Fluid Mechanics, 11, 69 (1982).

47) T. A. Hunt, B. D. Todd, Journal of Chemical Physics, 131, 054904 (2009).

48) G Ianniruberto, A. Brasiello, G Marrucci, Macromolecules, 45, 8058 (2012).

49) G. Ianniruberto, A. Brasiello, G Marrucci, Proceeding of 7th Annual European

Rheology Conference, 61 (2011).

50) J. K. Nielsen, H. K. Rasmussen, O. Hassager, Journal of Rheology, 52, 885 (2008).

51) K. Kremer, G. S. Grest, Journal of Chemical Physics, 92, 5057 (1990).

CHAPTER 2

Analysis of nonlinear stress relaxation data in literature

2-1. Introduction

As described in Chapter 1, the universality of polymer viscoelasticity fails under fast elongational flow,[1)-7)] and the stretch/orientation-induced friction reduction is one possible candidate of the mechanisms leading to this lack of universality. This Chapter attempts to experimentally extract such reduction defined for the friction of Kuhn segment. This attempt is based on a working hypothesis that the friction reduction for the Kuhn segment is not affected by the entanglement density but uniquely determined by a so-called stretch/orientation parameter and on another hypothesis that the segmental friction remains isotropic even when the friction reduction occurs. In the remaining part of this Chapter, these hypotheses are explained first, and then the friction reduction is estimated accordingly.

2-2. Working hypothesis

In polymer melts, the frictional interaction should weaken when the subchain (entanglement segments) are stretched and oriented to reduce their mutual overlapping. In contrast, in polymer solutions, the polymer-polymer friction would be similarly reduced but the solvent-polymer friction should be hardly affected by the subchain stretch/orientation because the solvent molecules move much faster than the subchain. Thus, the friction reduction defined for the Kuhn segment (basic constituent of the subchain) would be determined by the stretch/orientation averaged for the polymer and the solvent, if any. Specifically, the fully-oriented and fully-stretched subchain can be

chosen as the reference having the minimum friction. Then, as a *working hypothesis*, the friction coefficient of the Kuhn segment ζ is assumed to be uniquely determined by a so-called stretch/orientation factor F_{SO} defined with respect to this reference:

$$\zeta = \zeta(F_{so}) \quad \text{with} \quad F_{so} = \tilde{\lambda}^2 \bar{S} \quad \text{and} \quad \tilde{\lambda} = \lambda / \lambda_{max} \tag{2.1}$$

Here, λ is the (average) subchain stretch ratio defined with respect to the equilibrium state, and $\tilde{\lambda}$ is the reduced stretch ratio normalized to the fully stretched state ($\lambda = \lambda_{max}$). $\bar{S}$ is an orientational anisotropy averaged for the polymer and the solvent if any. Because the solvent molecules relax very quickly and should remain isotropic under experimentally accessible conditions, $\bar{S}$ is contributed only from the polymer and can be expressed as

$$\bar{S} = \phi_P S_P \tag{2.2}$$

where S_p and ϕ_p are the orientational anisotropy (order parameter) and the volume fraction of the polymer. Specifically, S_p can be taken as an eigenvalue of the orientation tensor $<\mathbf{uu}>$, with $\mathbf{u}$ being the unit tangential vector of the subchain and $<\ldots>$ indicating the ensemble average: For the uniaxial elongation in x direction, $S_p = < u_x^2 > - < u_y^2 >$ with u_x and u_y being components of $\mathbf{u}$ in x and y directions, respectively.

A comment needs to be made for the working hypothesis that chooses $F_{so} = \tilde{\lambda}^2 \bar{S}$ as the parameter uniquely determining the friction reduction. This F_{so} is the simplest measure of the orientation and correlation *averaged* for the Kuhn segments in the subchain and the solvent molecules. Namely, both S_p and $\tilde{\lambda}$ of the subchain become unity when all Kuhn segments therein are fully aligned in the direction of $\mathbf{u}$, and the friction coefficient ζ of the Kuhn segment should be most significantly reduced in this fully oriented/stretched state. The anisotropic solvent molecules should weaken this reduction. The simplest expression for this solvent effect is given by the average $\bar{S} = \phi_P S_P$ (Eq. 2.2) just counting the orientation of the subchain, which results in the simplest choice of

$F_{so} = \tilde{\lambda}^2 \bar{S}$ (Eq. 2.1) as the parameter uniquely determining the friction reduction.

Another comment needs to be made for Eq. 2.1. The flow-induced friction reduction could result in a tensorial form of the friction coefficient, with the reduction being stronger in the flow direction.[8] However, as the working hypothesis, Equation 2.1 assumes that the friction coefficient of the Kuhn segment remains isotropic even under fast flow and can be characterized by the scalar quantity, ζ.

2-3. Results and discussion

2-3-1. Acceleration of stress relaxation

Figure 2-1 shows the tensile stress relaxation data (σ_E^-) of monodisperse linear PS melt (M = 1.45×10^5; PS145K) at 393 K reported by Nielsen *et al.*[9] These data were measured after cessation of elongational flow in the transient hardening regime at strain rates $\dot{\varepsilon}$ = 0.001, 0.003, 0.01, and 0.03 s^{-1}; the flow time was chosen to achieve the same macroscopic Hencky strain for all rates, *i.e.*, ε_{flow} = 3.0 (elongation ratio = 20.1). The Rouse relaxation time of the chain is $\tau_R \cong 1.0 \times 10^3$ s,[9] and the Weissenberg number based on τ_R is $Wi_R = \dot{\varepsilon}\tau_R \cong$ 1, 3, 10, and 30 for those $\dot{\varepsilon}$ values. In the experiments, the σ_E^- value immediately after the flow cessation is not completely free from artifacts such as the shock (vibration) of the stretching device as well as inertia. Thus, in Fig. 2-1, the $\sigma_E^-(t)$ data are normalized by the data at short time (but still long enough to erase the effect of those artifacts), namely 1 s ($\ll \tau_R$), and plotted against the time t after the flow cessation. These $\sigma_E^-(t)/\sigma_E^-(1)$ data are useful to examine the effect of the pre-elongational rate $\dot{\varepsilon}$ on the stress decay behavior after the flow cessation.

Figure 2-1 clearly demonstrates that the increase of $\dot{\varepsilon}$ ($>1/\tau_R$) results in an acceleration of the decay of the $\sigma_E^-(t)/\sigma_E^-(1)$ ratio, particularly at short times. For the

highest $\dot{\varepsilon}$ (= 0.03 s^{-1}), an appreciable decay not seen at low $\dot{\varepsilon}$ starts at a very short time ($t \cong 2$ s). These results lend qualitative support to the mechanism of stretch/orientation-induced ζ-reduction. However, the finite extensibility (that leads to strain-hardening of the subchains) also contributes to this rapid decay at large $\dot{\varepsilon}$. Thus, a quantitative evaluation of the magnitude of the ζ-reduction requires detailed analysis of the $\sigma_E^-(t)/\sigma_E^-(1)$ data, as discussed below.

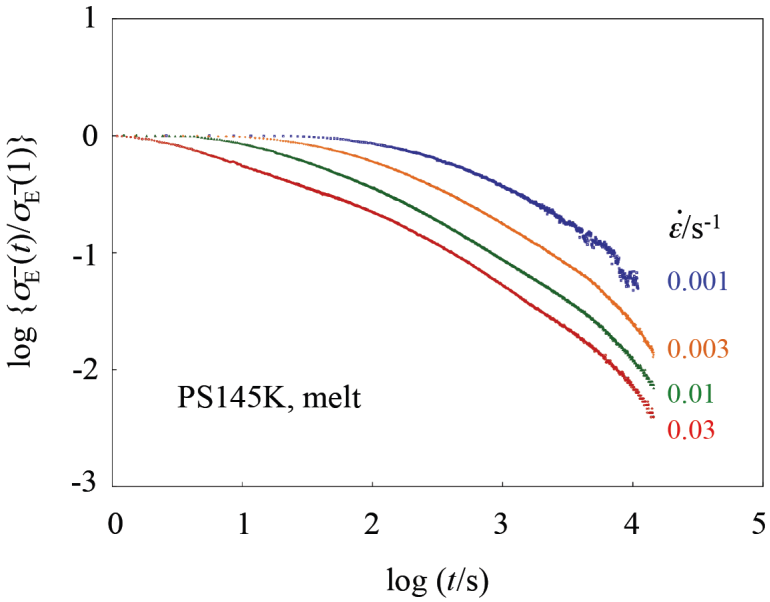

Figure 2-1 Stress decay data of PS145K melt[9] at 393 K after cessation of elongational flow (up to $\varepsilon_{flow} = 3$). Numbers indicate the strain rate.

The terminal relaxation, attributable to reptation explained in Chapter 1, should also dominate the nonlinear $\sigma_E^-(t)/\sigma_E^-(1)$ data at long times. This can be indeed observed in Fig. 2-1 where all curves become roughly parallel to one another at long times. Figure 2-2 confirms that the terminal relaxation process, occurring well after the Rouse-like chain retraction process, is insensitive to the pre-elongational rate $\dot{\varepsilon}$. Indeed, Figure 2-2 shows that the normalized ratio $h_E^{-1}\{\sigma_E^-(t)/\sigma_E^-(0)\}$ for various $\dot{\varepsilon}$ can be superposed at long

times with an adequate choice of the damping function h_E (with the data for $\dot{\varepsilon} = 0.001\ s^{-1}$ being used as the reference). This time-rate separability is analogous to the time-strain separability[10] under step strains.

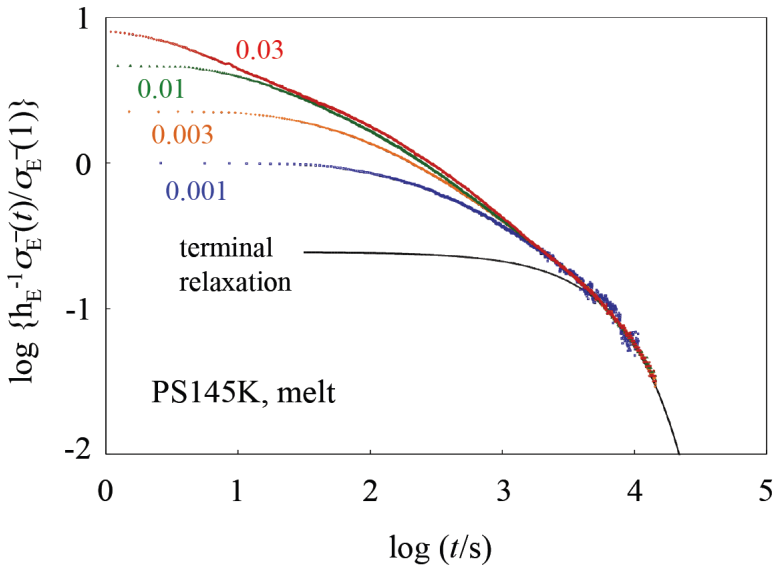

Figure 2-2 Test of time-rate factorability at long t for the stress decay data reported in Fig. 2-1. Numbers indicate the strain rate.

In Fig. 2-2, data at long times are well fitted by the single exponential, terminal relaxation function, $\{\sigma_E^-(t)/\sigma_E^-(1)\}_{terminal} = 0.245\exp(-t/\tau_d)$ with $\tau_d = 6.8\times10^3$ s. This terminal relaxation process somewhat contributes to the $\sigma_E^-(t)/\sigma_E^-(1)$ data even at short t, in particular for the case of the smallest $\dot{\varepsilon} = 0.001\ s^{-1}$. It is essential to subtract this contribution from the $\sigma_E^-(t)/\sigma_E^-(1)$ data for accurate examination of the fast relaxation process (Rouse-like chain retraction). The $\sigma_{E,fast}^-(t)/\sigma_{,E,fast}^-(1)$ ratio for the *fast* relaxation process obtained after this subtraction is shown in Fig. 2-3 together with the *linear* viscoelastic Rouse relaxation curve after flow cessation (dashed curve):

$$\frac{\sigma_{Rouse}^-(t)}{\sigma_{Rouse}^-(1)} = Q\sum_{p=1}^{N} g_p^R \exp\left(-\frac{p^2 t}{\tau_R}\right) \quad \text{with} \quad g_p^R = \frac{1}{p^2}\left\{1-\exp\left(-\frac{p^2 t_{flow}}{\tau_R}\right)\right\} \qquad (2.3).$$

Here, Q is a normalization factor ensuring that the ratio $\sigma^{-}_{\mathrm{Rouse}}(t)/\sigma^{-}_{\mathrm{Rouse}}(1)$ is unity at t = 1. Those Rouse relaxation curves were calculated with $\tau_{\mathrm{R}} = 10^3$ s (very close to the experimental τ_{R} data in the linear regime) and the experimental values of $\dot{\varepsilon}$ and the flow duration t_{flow}. (Equation 2.3 is straightforwardly obtained from the constitutive equation of the Rouse model,[10] and this constitutive equation is in turn deduced from the Rouse equation of motion explained in section 1-3-1.)

Figure 2-3 shows that the data for $\dot{\varepsilon}$ = 0.001 s^{-1} are very close to the dashed curve, suggesting that no friction reduction occurs in such a slow elongational flow. It also shows that the approximation of the terminal relaxation to a single exponential (as used in the subtraction) is acceptable even at short times. In contrast, the initial decay of the $\sigma^{-}_{\mathrm{E,fast}}(t)/\sigma^{-}_{\mathrm{E,fast}}(1)$ ratio due to chain retraction is considerably accelerated for all $\dot{\varepsilon}$ values larger than 0.001 s^{-1}, lending support to the mechanism of stretch/orientation-induced ζ-reduction.

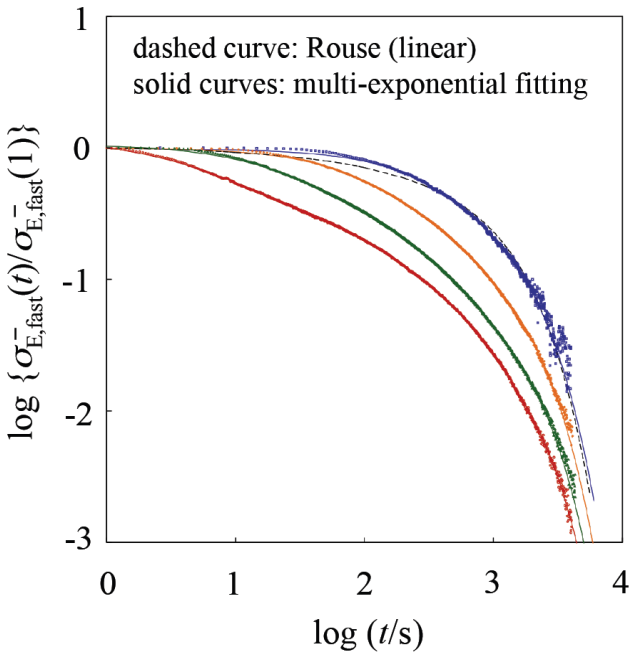

Figure 2-3 Same data as in Fig. 2-1 but after subtraction of the terminal relaxation. Solid curves are the result of fitting with a sum of exponential relaxation modes (see Table 2-1). Dashed curve is the Rouse relaxation curve of linear viscoelasticity, Eq. 2.1 with $t_{\rm flow} = 3 \times 10^3$ s.

Stress decay data after cessation of elongational flow have been reported also for two entangled semidilute PS solutions[2] at room temperature. The molecular weight M, concentration c, and solvent for the two solutions are $M = 10.2\times10^6$ (PS10.2M), c = 6 wt%, dibutyl phthalate, and $M = 3.9\times10^6$ (PS3.9M), c = 10 wt%, diethyl phthalate.[2] The PS10.2M solution was elongated at the rate $\dot{\varepsilon}$ = 1.0 s^{-1} (Wi_R = 3.0) up to three values of the Hencky strain, $\varepsilon_{\rm flow}$ = 2.0, 2.5, and 4.0, whereas the PS3.9M solution was elongated at $\dot{\varepsilon}$ = 11.7 s^{-1} (Wi_R = 3.3) up to $\varepsilon_{\rm flow}$ = 3.3, 4.0, and 4.6. These data were analyzed in the same way as for the PS145K melt to evaluate the tensile stress due to the fast relaxation process. The resulting $\sigma^-_{\rm E,fast}(t)$ data for the fast process were normalized by the stress value at a suitably short time t* (but still long enough to erase possible artifacts): t*=0.1s and t*=0.05s for the PS10.2M and PS3.9M solutions, respectively.

The $\sigma^{-}_{E,fast}(t)/\sigma^{-}_{E,fast}(t^*)$ ratios of the solutions thus obtained are shown in Figs. 2-4 and 2-5, together with the linear viscoelastic Rouse relaxation curve (after cessation of steady elongational flow; Eq. 2.3 with $g_p^R = 1/p^2$ for $t_{flow} >> \tau_R$). These solution data are insensitive to ε_{flow} and virtually superposed to the Rouse curve. Thus, the fast relaxation process of the solutions appears to exhibit no nonlinear acceleration observed for the melt, despite the fact that the data for solutions and melts cover similar values of Wi_R (~3) and ε_{flow} (~3). This result implies that the stretch/orientation-induced ζ-reduction is negligible for solutions under the experimental conditions examined.

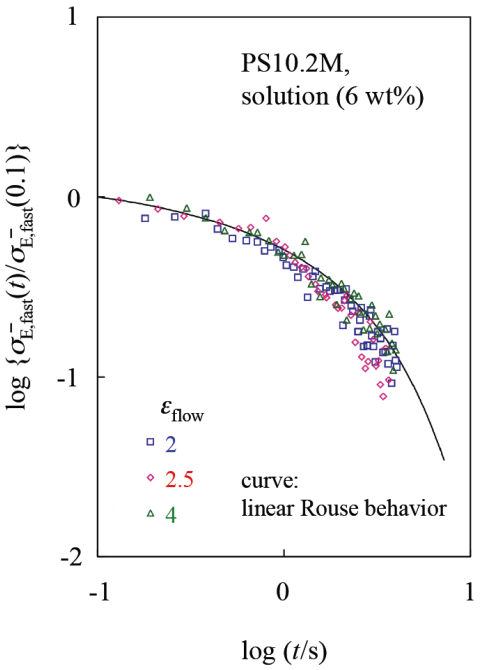

Figure 2-4 Stress decay during the fast relaxation process of the PS10.2M solution[2)] at 294 K after cessation of elongational flow at $\dot{\varepsilon}$ = 1.0 s^{-1}. The curve shows the ratio calculated from Eq. 2.3 with $g_p{}^R = 1/p^2$.

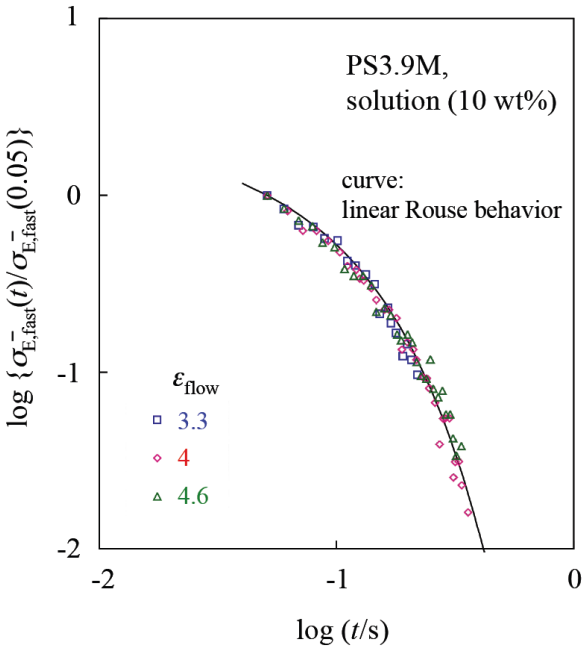

Figure 2-5 Stress decay during the fast relaxation process of the PS3.9M solution[2)] at 294 K after cessation of elongational flow at $\dot{\varepsilon}$ = 11.7 s^{-1}. The curve shows the ratio calculated from Eq. 2.3 with $g_p{}^R = 1/p^2$.

2-3-2. Empirical equation for stretch/orientation-induced monomeric friction reduction

The $\sigma^{-}_{E,fast}(t)/\sigma^{-}_{E,fast}(t^*)$ curves for the fast process of PS145K (Fig. 2-3) appear to be parallel to one another at long times, suggesting that the time-rate separability holds also for this process at long times. Validity of this separability is examined in Fig. 2-6(a) where those $\sigma^{-}_{E,fast}(t)/\sigma^{-}_{E,fast}(t^*)$ data are reduced by a suitable damping function $h_{E,fast}$ and semi-logarithmically plotted against time. All data sets show unambiguously the same "terminal" relaxation time $\tau_{1,fast}$ (reciprocal of the slope in the semi-logarithmic plot at long times), and hence satisfy the separability.[10] In addition, $\tau_{1,fast}$ (= 1.1×10^3 s) agrees well with the Rouse time of PS145K, $\tau_R \cong 1.0\times10^3$ s, reported by Nielsen *et al.*[9] This result reveals that at times of the order of τ_R the friction coefficient after cessation of fast elongational flow is the same as at equilibrium, which indeed is reasonable because any possible effect of the chain stretch would have relaxed over that time scale. In contrast, the relaxation in short time scales is much faster for cessation of faster elongational flow, as noted in Figs. 2-6(a) and 2-3.

It may sound tempting to evaluate the magnitude of the acceleration (attributable to decrease of the friction coefficient of the Kuhn segment) from the initial decay rate of the $\sigma^{-}_{E,fast}(t)/\sigma^{-}_{E,fast}(t^*)$ data. However, this evaluation method is not adequate because of the multi-mode nature of the relaxation at short times. The initial stress decay rate changes even for the Rouse relaxation in the linear viscoelastic regime unless t_{flow} is much longer than τ_R, as noted from Eq. 2.3: The mode intensities g_p^R change with t_{flow} unless $t_{flow} >> \tau_R$, and those changes contribute to the initial relaxation rate of $\sigma^{-}_{E,fast}(t)/\sigma^{-}_{E,fast}(t^*)$. Therefore, it is essential to conduct a multi-mode analysis of the data in Fig. 2-3 or Fig. 2-6(a). Such analysis is executed by fitting the data with a sum of exponentially decaying modes given as

$$\frac{\sigma_{\mathrm{E}}^{-}(t)}{\sigma_{\mathrm{E,fast}}^{-}(t^{*})} = \sum_{p\geq 1} g_p \exp\left(-\frac{t}{\tau_{\mathrm{p}}}\right) \tag{2.4}$$

In Eq. 2.4, the slowest mode has the relaxation time τ_1 (= 1.1×10^3 s as determined in Fig. 2-6(a) for all $\dot{\varepsilon}$ values). The normalized relaxation intensity g_1 of this mode is determined from the data in Fig. 2-6(a) as well. The relaxation time and normalized intensity of higher order modes, τ_p and g_p with $p \geq 2$, can be determined experimentally, from slower mode to faster mode, by the procedure X:[11] In this procedure, τ_2 and g_2 are determined from the terminal decay behavior of $\sigma_{\mathrm{E}}^{-}(t)/\sigma_{\mathrm{E,fast}}^{-}(t^{*}) - g_1\exp(-t/\tau_1)$, where τ_1 and g_1 have been determined from the terminal tail of the $\sigma_{\mathrm{E}}^{-}(t)/\sigma_{\mathrm{E,fast}}^{-}(t^{*})$ data in Fig. 2-6(a). The τ_2 and g_2 thus obtained are utilized to determine $\tau_{3,\mathrm{fast}}$ and g_3 from the terminal tail of $\sigma_{\mathrm{E}}^{-}(t)/\sigma_{\mathrm{E,fast}}^{-}(t^{*}) - g_1\exp(-t/\tau_1) - g_2\exp(-t/\tau_2)$, and τ_p and g_p of higher order modes are sequentially determined from τ_q and g_q of lower order modes (with $q < p$) within experimental resolution. The parameters thus determined are summarized in Table 2-1. The corresponding curves (Eq. 2.4) excellently describe the data, as shown with the solid curves in Fig. 2-3.

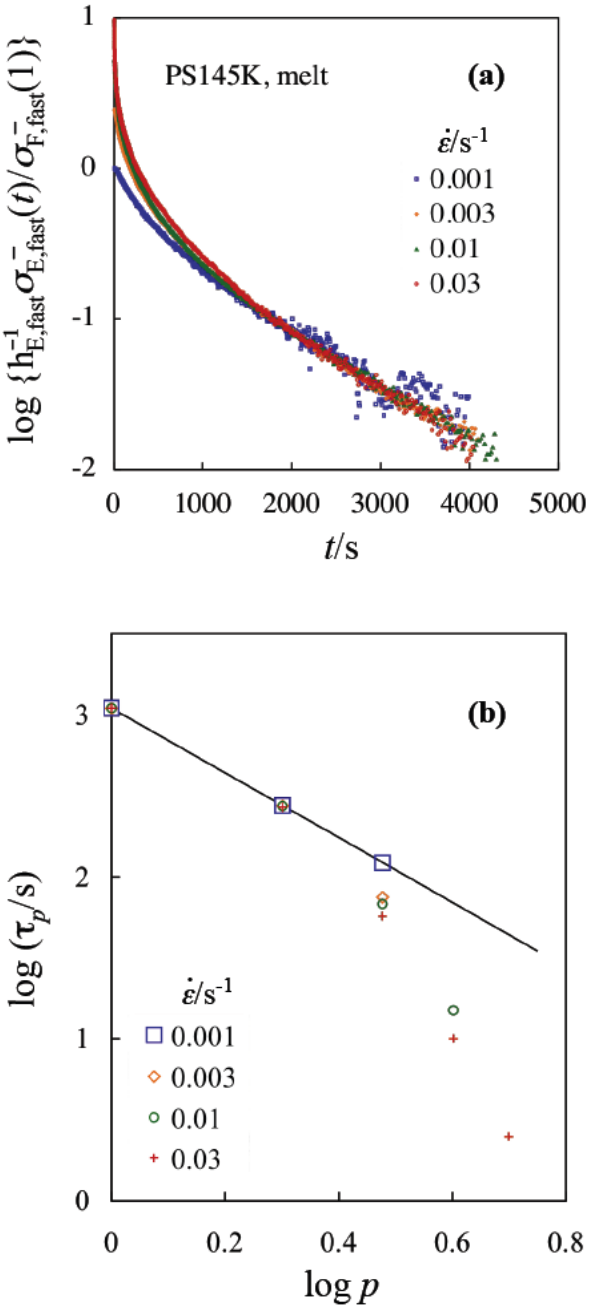

Figure 2-6 (a) Same data as in Fig. 2-3 vertically shifted to test time-rate separability at long times. (b) Characteristic times of the multi-exponential fit of the data in Fig. 2-3. The straight line is Eq. 2.5.

Table 2-1 Parameters of the multi-exponential relaxation

$\dot{\varepsilon}$ /s^{-1}	τ_p/s					g_p				
	p=1	p=2	p=3	p=4	p=5	p=1	p=2	p=3	p=4	p=5
0.001	1100	275	122			0.485	0.50	0.05		
0.003	1100	275	75			0.210	0.37	0.42		
0.01	1100	273	68	15		0.096	0.23	0.36	0.37	
0.03	1100	270	57	10	2.5	0.055	0.16	0.215	0.41	0.30

The τ_p thus determined are double-logarithmically plotted against p in Fig. 2-6(b). For the smallest $\dot{\varepsilon}$ = 0.001 s^{-1}, τ_p is well described by the Rouse relationship shown as the solid line in Fig. 2-6(b);

$$\tau_p = \frac{1.1\times10^3}{p^2} \text{ (in s)} \qquad (2.5).$$

This result is in harmony with the close coincidence between the Rouse curve and the $\bar{\sigma}_{E,fast}(t)/\bar{\sigma}_{E,fast}(1)$ data for this $\dot{\varepsilon}$ shown in Fig. 2-3. However, Figure 2-6(b) also demonstrates that τ_p for the higher order modes (with $p \geq 3$) at larger $\dot{\varepsilon}$ deviates downwards from the Rouse scaling of Eq. 2.5. In Fig. 2-6(b), the τ_p's for the lower order modes remain proportional to p^{-2} and thus the relaxation of those modes is not accelerated even at large $\dot{\varepsilon}$. This result suggests that the relaxation is accelerated only when the (entangled) subchains are highly stretched: The stretch relaxes significantly through the higher order modes so that the acceleration vanishes in the time scale of lower order modes.

The accelerated relaxation of the higher order modes is attributed to the stretch/orientation-induced reduction of the monomeric friction coefficient ζ as well as to the finite-extensible nonlinear elasticity (FENE).[12] Thus, $\tau_p(\dot{\varepsilon})/\tau_p(0)$ ratio for the highest order mode resolved experimentally (p = 3, 4, and 5 for $\dot{\varepsilon}$ = 0.003, 0.01, and 0.03 s^{-1}), with $\tau_p(0)$ being given by the Rouse scaling (Eq. 2.5 and solid line in Fig. 2-6(b)), can be related to the $\zeta(F_{so})/\zeta(0)$ ratio and the FENE factor $f_{FENE} = \kappa(F_{so})/\kappa(0)$, with κ being the spring constant of the entangled strand, as

$$\frac{\tau_p(\dot{\varepsilon})}{\tau_p(0)} = \frac{1}{f_{FENE}} \frac{\zeta(F_{so})}{\zeta(0)} \tag{2.6}$$

The stretch/orientation parameter F_{so} ($= \tilde{\lambda}^2 \bar{S}$) appearing in Eq. 2.6 can be related, with the decoupling approximation, to the elongational stress $\sigma_E(\dot{\varepsilon})$ just before the cessation of elongational flow as

$$\sigma_E = 3\nu_e k_B T f_{FENE} \lambda^2 S_P = 3\nu_{e0} \frac{n_0}{n} k_B T f_{FENE} \tilde{\lambda}^2 \lambda_{max}^2 \frac{\bar{S}}{\phi_P} = \frac{3G_e n_0}{\phi_P} f_{FENE} F_{so} \tag{2.7}$$

Here, ν_e is the number density of entangled subchains and ν_{e0} is its equilibrium value, n is the number of Kuhn segment per entangled subchain and n_0 is its equilibrium value: These parameters satisfy a relationship, $\nu_e = \nu_{e0} n_0/n$. k_B and T are the Boltzmann constant and absolute temperature, respectively, and $G_e = \nu_0 k_B T$ is the plateau modulus in the linear viscoelastic regime. (Equations 2.1 and 2.2 and a characteristic relationship $\lambda_{max}^2 = n_0$ were utilized to derive Eq. 2.7)

The f_{FENE} factor appearing in Eqs. 2.6 and 2.7 cannot be directly evaluated from the elongational $\sigma_E(\dot{\varepsilon})$ data. For this reason, the above experimental analysis alone cannot make direct plots of the $\zeta(F_{so})/\zeta(0)$ ratio against F_{so}. Nevertheless, a product $F_{so} f_{FENE} = \sigma_E \phi_P/(3G_e n_0)$ (Eq. 2.7) can be evaluated from the $\sigma_E(\dot{\varepsilon})$ data together with the known

values of G_e, ϕ_P, and n_0 (= $15\phi_P^{-1.3}$ where the prefactor of "15" is the n_0 value known for bulk PS[13]). For the PS melt[9] and the two solutions,[2] Figure 2.7 shows plots of $\{\zeta(F_{so})/\zeta(0)\}/f_{FENE}$ (= $\tau_p(\dot{\varepsilon})/\tau_p(0)$ data; *cf.* Eq. 2.6) against the product $F_{so}f_{FENE}$ thus evaluated. The plots for the melt and solutions appear to cover a common master curve in different ranges of $F_{so}f_{FENE}$, and the $F_{so}f_{FENE}$ value in the range covered by the solution data appears to be too small to activate the stretch/orientation-induced ζ-reduction. This result is in harmony with the discussion made for Figs. 2-3, 2-4, and 2-5.

For convenience of multi-chain simulation conducted later in Chapter 3, it is desired to convert the plots in Fig. 2-7 in an empirical equation. The solid curve shown therein indicates the empirical equation fitted for this purpose,

$$\frac{\zeta(F_{so})}{\zeta(0)}\frac{1}{f_{FENE}} = \frac{1}{(1+\beta)^{\gamma}}\left\{\beta + \frac{1-\tanh\alpha\left(F'_{so}-F'^{*}_{so}\right)}{2}\right\}^{\gamma} \qquad (2.8),$$

with

$$F'_{so} \equiv F_{so}f_{FENE} = \sigma_E\phi_P/(3G_en_0) = \sigma_E\phi_P M_K/(3\rho RT) \qquad (2.9).$$

Here M_K is the Kuhn molar mass. In Eq. 2.8, F'^{*}_{so} (= 0.14) is the threshold value for the onset of the stretch/orientation-induced reduction of ζ, while α (= 20) and γ (= 0.15) specify how rapidly ζ decreases with increasing F_{so}. The remaining parameter, β (= 5.0×10^{-9}), specifies the asymptotic value of $\{\zeta(F_{so})/\zeta(0)\}/f_{FENE}$ (= $\{\beta/(1+\beta)\}^{\gamma}$ for large F_{so}.).

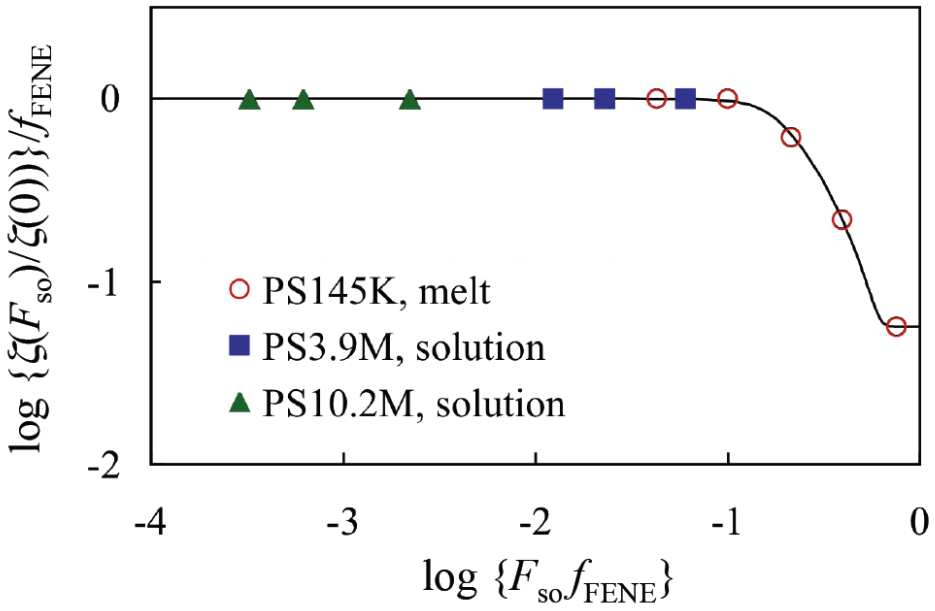

Figure 2-7 Plot of $\{\zeta(F_{so})/\zeta(0)\}/f_{FENE}$ ($=\tau_p(\dot{\varepsilon})/\tau_p(0)$ for the highest p available in Fig. 2-6(b) for the melt, and =1 for solutions) against $F_{so}f_{FENE}$ ($=\sigma_E\phi_P/3G_en_0$). The fitting curve is Eq. 2.8.

2-4. Conclusions

Literature data of the stress relaxation after cessation of transient elongational flow reported for a PS melt and two PS solutions were analyzed to estimate changes of the Kuhn segment friction ζ due to flow. In a working hypothesis, ζ was expressed as a function of an orientation/stretch factor $F_{so} = \tilde{\lambda}^2 \overline{S}$ with $\tilde{\lambda}$ (= λ/λ_{max}) being a reduced stretch ratio of the entangled subchain (entanglement segment) defined with respect to the full-stretch limit ($\lambda = \lambda_{max}$), and $\overline{S}$, an average orientational anisotropy of the components (polymer and solvent, if any). From the stress relaxation data, the $\zeta(F_{so})/\zeta(0)$ ratio was obtained as an implicit function of F_{so}. This function shows the decrease of $\zeta(F_{so})$ on an increase of $F_{so} > 0.14$.

References

1) P. K. Bhattacharjee, J. P. Oberhauser, G. H. McKinley, L. J. Leal, T. Sridhar, Macromolecules, 35, 10131 (2002).

2) P. K. Bhattacharjee, D. A. Nguyen, G. H. McKinley, T. Sridhar, Journal of Rheology, 47, 269 (2003).

3) X. Ye, R. G. Larson, C. Pattamaprom, T. Sridhar, Journal of Rheology, 47, 443 (2003).

4) A. Bach, K. Almdal, H. K. Rasmussen, O. Hassager, Macromolecules, 36, 5174 (2003).

5) C. Luap, C. Muller, T. Schweizer, D. C. Venerus, Rheologica Acta, 45, 83 (2005).

6) Q. Huang, O. Mednova, H. K. Rasmussen, N. J. Alvarez, A. L. Skov, K. Almdal, O. Hassager, Macromolecules, 46, 5026 (2013).

7) T. Sridhar, M. Acharya, D. A. Nguyen, P. K. Bhattacharjee, Macromolecules, 47, 379 (2014).

8) T. Uneyama, K. Horio, H. Watanabe, Physical Review E, 83, 001800 (2011).

9) J. K. Nielsen, H. K. Rasmussen, O. Hassager, Journal of Rheology, 52, 885 (2008).

10) M. Doi, S. F. Edwards, *"The theory of polymer dynamics"*, Oxford University Press Inc, Clarendon (1986).

11) H. Sobue, K. Murakami, Kogyo Kagaku Zasshi, 64, 2005 (1961).

12) H. R. Warner, Industrial and Engineering Chemistry Fundamentals, 11, 379 (1972).

13) M. Rubinstein, R. Colby, *Polymer Physics*, Oxford University Press Inc, Oxford (2003).

CHAPTER 3

Uniaxial elongational viscoelastic behavior investigated through a multi-chain model

3-1. Introduction

The multi-chain nature of the entanglement dynamics is considered in the tube model as the thermal and convective constraint release (TCR and CCR) processes within the mean-field, single chain approximation. However, validity of this approximation is not fully established and sometimes questionable. In contrast, the Primitive Chain Network (PCN) model[1)] includes no such single-chain approximation, and its prediction incorporating *no* stretch/orientation-induced friction reduction is quantitatively consistent with the universal viscoelastic functions for entangled polymers under shear.[2)] However, the PCN model with no friction reduction cannot describe the uniaxial elongational behavior for PS melts.[3)]

For this problem, this Chapter conducts the PCN simulation incorporating the friction reduction. For this purpose, the empirical equation for the friction reduction obtained in Chapter 2 is combined with the PCN simulation. The method and results of the simulation are described below.

3-2. Model

In the PCN model,[1)] polymer chains are coarse grained at the level of the entanglement molecular weight, and each chain is replaced by a sequence of subchains connecting consecutive entanglements. Those coarse-grained chains are similar to the primitive chains of tube theory. The PCN model represents the entanglements as

sliplinks, *i.e.*, small links through which monomers of one subchain can be transferred to the neighboring subchains. Based on an assumption of binary topological interaction, each sliplink binds a pair of subchains. The whole system is modeled as a network of Gaussian chains bound by sliplinks, and these chains are allowed to move/relax through reptation/CLF (through the sliplinks), as well as through CCR and TCR induced by removal and creation of sliplinks. Dynamics of the network results from motion of the node (formed by four subchains bound at the sliplink) and of the free end of the chain, the monomer transport through sliplinks, and creation/destruction of sliplinks due to hooking/unhooking processes between chains.

The state valuables for description in the PCN model are the position vector of the sliplinks $\{\mathbf{R}\}$, number of monomers per subchain $\{n\}$, and number of subchains per chain $\{Z\}$.

The time evolution of $\{\mathbf{R}\}$ and $\{n\}$ are given by the following 3D and 1D Langevin equations, respectively:

$$(\zeta_{s1} + \zeta_{s2})(\dot{\mathbf{R}} - \boldsymbol{\kappa} \cdot \mathbf{R}) = \sum_{i}^{4} \mathbf{F}_i + \mathbf{F}_f + \mathbf{F}_B \tag{3.1},$$

$$\frac{\zeta_s}{\rho} \dot{n} = (F_i - F_{i-1}) + f_f + f_B \tag{3.2}.$$

The LHS of Eq. 3.1 is the node friction force, where $\dot{\mathbf{R}}$ is the time derivative of $\mathbf{R}$ and $\boldsymbol{\kappa}$ is the externally imposed velocity gradient tensor. The subchain friction coefficient ζ_s is given by

$$\zeta_s = < n_i > \zeta(F_{so}) \tag{3.3}.$$

Here $< n_i >$ is the number of monomers in the subchain averaged along each chain. $\zeta(F_{so})$ is the friction coefficient of a monomer (Kuhn segment) depending on the

stretch/orientation factor F_{so} defined by Eq. 2.1 as discussed in Chapter 2. Equation 3.3 accounts for changes of monomer number n in the subchains due to fluctuations in the number of entanglements. This fluctuation is especially important under fast flow because of CCR.

In Eq. 3.1, ζ_{s1} and ζ_{s2} each refer to one of the two subchains forming the binary entanglement. The overall chain friction coefficient stays constant as it should, *given that* the monomeric friction coefficient ζ_s is constant. The RHS of Eq. 3.1 includes all other forces acting on the node, namely, the elastic forces $\mathbf{F}_i$ from the 4 subchains converging into the node, the Brownian force $\mathbf{F}_B$, and a field force $\mathbf{F}_f$ due to the incompressibility constraint. $\mathbf{F}_B$ is of thermal origin and related to ζ_s through the fluctuation-dissipation theorem,[4] *i.e.*, $\langle \mathbf{F}_B(t)\mathbf{F}_B(t') \rangle = 2(\zeta_{s1}+\zeta_{s2})k_BT\delta(t-t')\mathbf{I}$ ($\mathbf{I}$ = unit tensor).

The elastic force $\mathbf{F}_i$ is expressed as the entropic spring force with the nonlinear finite extensibility (FENE):[3]

$$\mathbf{F}_i = f_{\mathrm{FENE}} \frac{3k_BT}{n_i b^2}\mathbf{r}_i \tag{3.4}.$$

Here, k_BT is the thermal energy, n_i is the number of monomers of i-th subchain having the end-to-end vector $\mathbf{r}_i$, and b indicates the Kuhn monomer length. If the subchain is treated as the infinitely extensible Gaussian chain (as in the original PCN code), the factor f_{FENE} appearing in Eq. 3.4 is given by:[1]

$$f_{\mathrm{FENE}} = 1 \tag{3.5}.$$

On the other hand, for the actual subchains with the finite extensibility, f_{FENE} can be expressed within the FENE-P approximation[5] as[3]

$$f_{\mathrm{FENE}} = \frac{1}{1-\left\langle (r_i / r_{i,\max})^2 \right\rangle_i} \quad \text{with} \quad r_i = |\,\mathbf{r}_i\,| \tag{3.6}.$$

Here, $r_{i,\max}$ ($=bn_i$) is the full-stretch length of i-th subchain. This $r_{i,\max}$ depends on the monomer number per entangled segment and thus increases on loss of entanglements due to CCR under fast flow. The use of FENE-P rather than FENE eliminates numerical difficulties due to overstretched segments that are artificially generated by Brownian kicks and/or conformational rearrangements upon creation of sliplinks.[6] Obviously, the difference between Eqs. 3.5 and 3.6 has a significant effect on the PCN simulation results only when the subchains are considerably stretched (by fast uniaxial elongational flow, for example). The field force $\mathbf{F}_{\mathrm{f}}$ is related to the chemical potential μ as

$$\mathbf{F}_{\mathrm{f}} = -\nabla\mu \tag{3.7}.$$

The free energy A, giving μ as a derivative, is of the simple form:[7]

$$A = \begin{cases} \varepsilon\left(\dfrac{\phi}{\langle\phi\rangle} - 1\right)^2 & \text{for } \phi > \langle\phi\rangle \\ 0 & \text{for } \phi \le \langle\phi\rangle \end{cases} \tag{3.8}.$$

Here ϕ is the local subchain density, $\langle\phi\rangle$ is the average of ϕ in the whole system, and ε is a numerical factor specifying the magnitude of $\mathbf{F}_{\mathrm{f}}$ (ε was fixed at 0.5).

In Eq. 3.2 describing the time evolution of $\{n\}$, the time derivative $\dot{n}$ indicates the rate of change of n_i due to sliding of monomers from the (i-1)-th to the i-th subchain, ρ is the linear monomer density, and F_i denotes the subchain tension given through the scalar equivalent of Eq. 3.4:

$$\mathrm{F}_i = f_{\mathrm{FENE}} \frac{3kT}{n_i b^2} r_i \tag{3.9}.$$

f_f and f_B also appearing in Eq. 3.2 are the osmotic force between the (i-1)-th to the i-th subchain and the random force characterized by $< f_B(t) f_B(t') >= 2\zeta_s k_B T \delta(t-t')$.

Finally, the time evolution of $\{Z\}$ occurs through loss or creation of sliplink (entanglement) near the chain ends. In the simulation, a new sliplink is created if the monomer number in the end subchain n becomes larger than $1.5n_0$ whereas the existing sliplink is removed if $n < 0.5n_0$, where n_0 is the average monomer number per subchain at equilibrium.

The stretch/orientation-induced monomeric friction reduction incorporated in the simulation is described by the empirical function obtained in Chapter 2,

$$\frac{\zeta(F_{so})}{\zeta(0)} = f_{FENE} \frac{1}{(1+\beta)^{\gamma}} \left\{ \beta + \frac{1-\tanh \alpha (F_{so} f_{FENE} - F_{so}^*)}{2} \right\} \qquad (3.10).$$

(Equation 3.10 is equivalent to Eq. 2.8.) The parameters are: $\alpha = 20$, $\beta = 5 \times 10^{-9}$, $\gamma = 0.15$ and $F_{so}^* = 0.14$. For the uniaxial elongational flow in z direction, the stretch/orientation factor F_{so} appearing in Eq. 3.10 is given by

$$F_{so} = \frac{\sigma_{zz} - \sigma_{xx}}{3 G_0 n_0 f_{FENE}} \qquad (3.11),$$

where $\sigma_{zz} - \sigma_{xx} = \sigma_E$, G_0 is the unit modulus of the PCN model, and n_0 is the equilibrium number of Kuhn segment per subchain, as explained in Chapter 2.

Based on the stress optical law,[8] the stress tensor in the PCN model is written as

$$\boldsymbol{\sigma} = \frac{1}{V_{box}} \sum \mathbf{F}_i \mathbf{r}_i \qquad (3.12),$$

with V_{box} being the total volume of simulation box. Equation 3.12 is rewritten in terms of state variable as

$$\boldsymbol{\sigma} = 3G_0 n_0 f_{\mathrm{FENE}} \frac{Z}{Z_0} \left\langle \frac{\mathbf{rr}}{n} \right\rangle \tag{3.13},$$

where Z/Z_0 is the ratio of the current (average) subchain number per chain to its equilibrium value, and $\mathbf{r}$ is the nondimensional subchain end-to-end vector. $\boldsymbol{\sigma}$ given by Eqs. 3.12 and 3.13 has no contribution from the field forces $\mathbf{F}_{\mathrm{f}}$ (Eq. 3.7), because such contribution remains isotropic and small compared to that from elastic forces $\mathbf{F}_i$.

In the simulation, Equations 3.1 and 3.2 are nondimensionalized by using the equilibrium distance a between consecutive entanglements as the unit length, and the subchain equilibrium relaxation time $\tau_0^{\mathrm{PCN}} = n_0 \zeta(0) a^2 / 6k_{\mathrm{B}}T$ as the unit time. These equations are integrated numerically using a simple Euler-type integration scheme. Although Equations 3.1 and 3.2 are integrated with a time step much smaller than τ_0^{PCN} for obvious numerical reasons, the results are meaningful only every subchain characteristic time τ_0^{PCN} because of the coarse graining in the PCN model at the level of the length scale a. In contrast, the variable friction coefficient (Eq. 3.10) is updated at every τ_0^{PCN} and kept constant in between.

A comment needs to be made for the friction reduction factor given by Eq. 3.10. Differing from the experimental analysis explained in Chapter 2, the FENE factor f_{FENE} (Eq. 3.6) is directly evaluated from the subchain conformation in the simulation, and the stretch/orientation factor F_{so} (Eq. 3.11) is obtained accordingly. Thus, the friction reduction factor can be explicitly calculated in the simulation (and renewed in every τ_0^{PCN}).

3-3. Simulations

In the simulation, the periodic boundary condition was used and the number of subchains *per* unit volume was set to to be 10 (under equilibrium). For uniaxial deformation, a flat simulation box of the size 4x104x104, with 4 in the stretching direction, was used as the starting box, and the simulation was stopped when a steady flow was achieved or when the box elongational ratio Λ reached the maximum value $\Lambda_{max} = 676$ (*i.e.*, when the deformed box became 2704x4x4) corresponding to an Hencky strain ($\varepsilon_H = \ln\Lambda$) of ca. 6.5. The starting box was equilibrated under quiescent conditions for a sufficiently long time (longer than the longest relaxation time of the system). For a chain with molecular weight M, the number of subchains per chain is given by $Z_0 = M / M_0$, with M_0 being the average molecular weight of the subchains. The average monomer number per subchain, n_0, was calculated from the Kuhn molar mass M_K as $n_0 = M_0 / M_K$. The length of the fully stretched subchain is given by $r_{i,\max} = bn_i$ and its nondimensional form is given by $\tilde{r}_{i,\max} = bn_i / b\sqrt{n_0} = n_i / \sqrt{n_0}$.

The basic simulation parameters of the PS systems were evaluated through comparison between the simulation results and linear viscoelastic data of PS solution[9] and melts.[10),11),12)] These parameters are summarized in Table 3-1 together with the values of M and T. The Rouse relaxation time of the chains, τ_R, also reported in Table 3-1, is linked to τ_0^{PCN} as $\tau_R = (Z_0^2 / 2\pi^2)\tau_0^{PCN}$. M_K for PS is assumed to be 720.[13)]

Table 3-1 Parameters of PS samples

Sample	Ref.	M	Z_0	n_0	T / K	G_0 /Pa	τ_0^{PCN} /s	τ_R /s
PS3.9M 10wt% sol.	9	3.9×10^6	33	160	294	2.0×10^3	7.0×10^{-3}	3.9×10^{-1}
PS100K	11	1.0×10^5	9	15	403	2.9×10^5	5.6	2.3x 10
PS200K	10	2.0×10^5	18	15	403	2.9×10^5	5.6	9.1x 10
PS390K	10	3.9×10^5	35	15	403	2.9×10^5	5.6	3.5×10^2
PS145K	12	1.45×10^5	13	15	403	2.9×10^5	140	1.2×10^3
PS200K-S	15	2.0×10^5	18	15	448	3.3×10^5	5.6×10^{-3}	9.2×10^{-2}

3-4. Results and discussion

3-4-1. Overview of uniaxial elongational behavior

For the case of solution for which the polymer concentration is small, the stretch/orientation parameter F_{so} appearing in Eq. 3.10 does not exceed the threshold value (0.14) and thus no frictional reduction occurs. Thus, the previous PCN simulation without the friction reduction reasonably described the elongational behavior of such solution, as shown in Ref. 3 for PS3.9M 10% solution. In contrast, this was not the case for PS melts. Thus, this chapter focuses on the uniaxial elongational behavior of PS melts.

Figure 3-1 shows the elongational viscosity growth function $\eta_E^+(t,\dot{\varepsilon})$ (up to the steady state) for PS100K,[11] PS200K[10] and PS390K[10] melts. The PCN-FENE simulation without the friction reduction (dashed curves) overestimates the $\eta_E^+(t,\dot{\varepsilon})$ data (symbols) at high $\dot{\varepsilon}$ ($>> \tau_R^{-1}$) and and at long times, as noted previously.[3] Incorporation of the

friction reduction in the simulation (solid curves) significantly improves agreement with the data. This improvement is most clearly noticeable for the PS390K melt (bottom panel).

Figure 3-2 compares strain rate ($\dot{\varepsilon}$) dependence of the simulated steady state viscosity $\eta_E(\dot{\varepsilon})$ with that of the data for PS100K,[11] PS200K[10] and PS390K[10] melts. The viscosity obtained from the PCN simulation without the friction reduction (thin dotted curves) shows thickening and is qualitatively different from the data. However, the simulation with the friction reduction well mimics the monotonic thinning of the $\eta_E(t,\dot{\varepsilon})$ data.

Figure 3-3 shows plots of the friction reduction factor $\zeta(F_{so})/\zeta(0)$ against the stretch/orientation parameter F_{so} obtained from the PCN simulation. (Differing from experiments, the simulation explicitly gives this plot, as explained earlier in section 3-2.) The plots obtained for various systems collapse on a master curve, which suggests that the $\zeta(F_{so})/\zeta(0)$ ratio is essentially (though perhaps not rigorously) a function of the single parameter F_{so}. It is also noted that the $\zeta(F_{so})/\zeta(0)$ ratio sharply decreases on an increase of F_{so} above a threshold value (= 0.14). This relationship between $\zeta(F_{so})/\zeta(0)$ and F_{so} is qualitatively similar to the empirical relationship between $\{\zeta(F_{so})/\zeta(0)\}/f_{FENE}$ and $F_{so}f_{FENE}$ shown in Fig. 2-7.

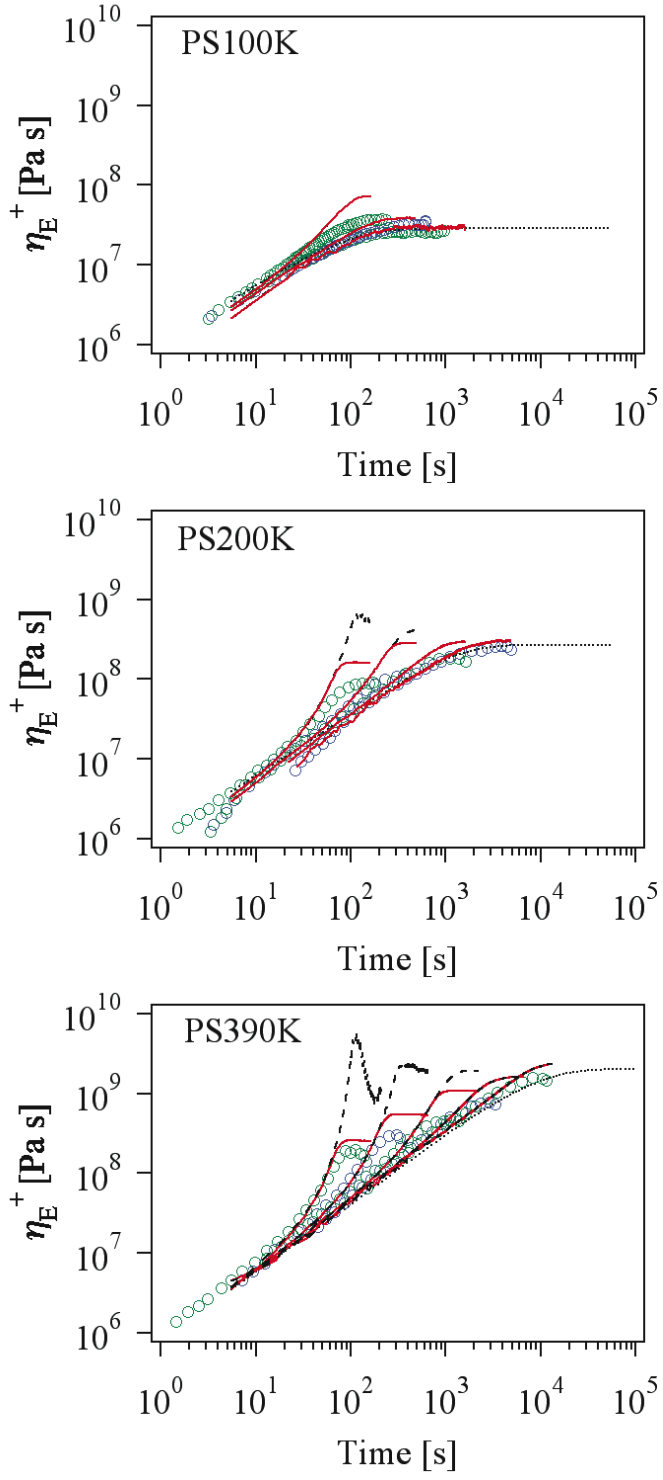

Figure 3-1 Uniaxial viscosity growth function for PS100K,[11] PS200K[10] and PS390K[10] melts at 403 K. The strain rates are 0.003, 0.01 and 0.03 s^{-1} for PS100K, 0.001, 0.003, 0.01 and 0.03 s^{-1} for PS200K and 0.0003, 0.001, 0.003, 0.01 and 0.03 s^{-1} for PS390K. Experimental data are shown with symbols. Dashed and solid curves, respectively, indicate the PCN-FENE simulation results without and with the stretch/orientation-induced monomeric reduction of friction. Dotted curve is the linear viscosity growth function.

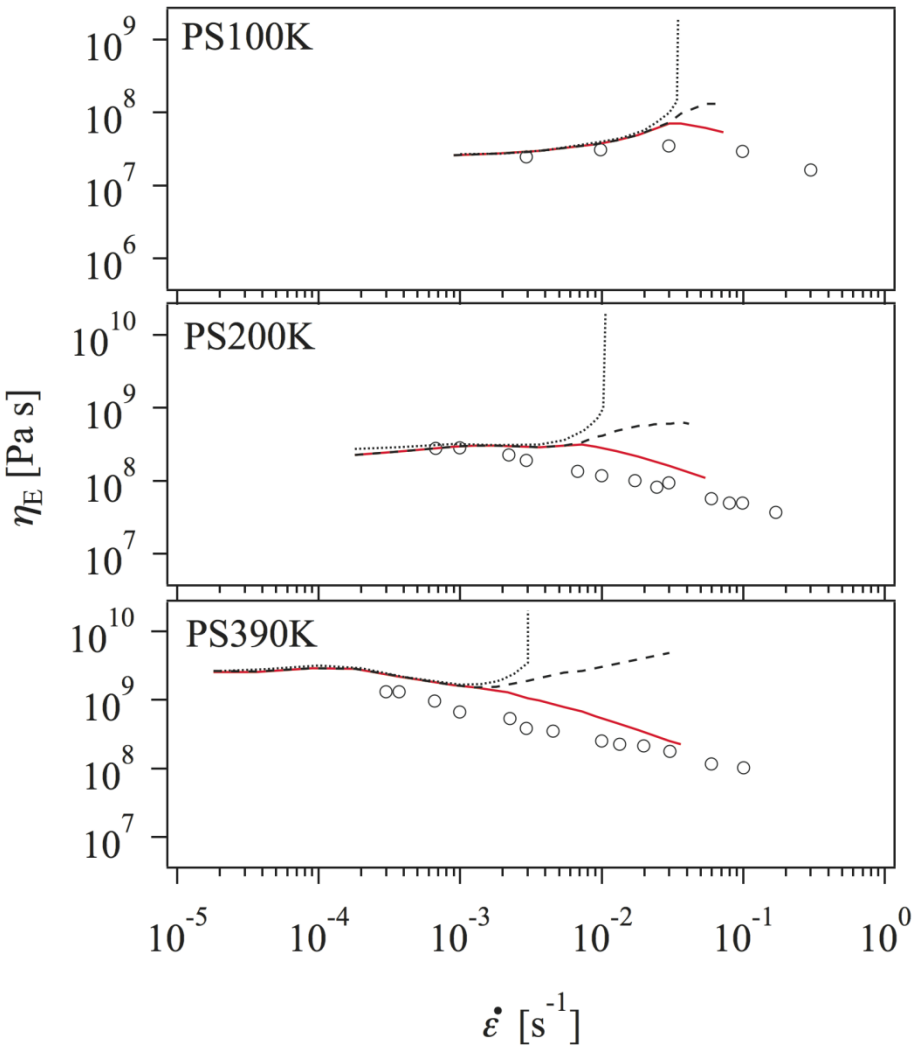

Figure 3-2 Steady state elongational viscosity for PS100K,[11] PS200K[10] and PS390K[10] at 403 K plotted against strain rate. The PCN simulation results without FENE and ζ reduction are shown with thin dotted curves. The PCN-FENE results without and with the stretch/orientation-induced monomeric reduction of friction are indicated with thick dashed and solid curves, respectively. Experimental data are shown with unfilled circles.

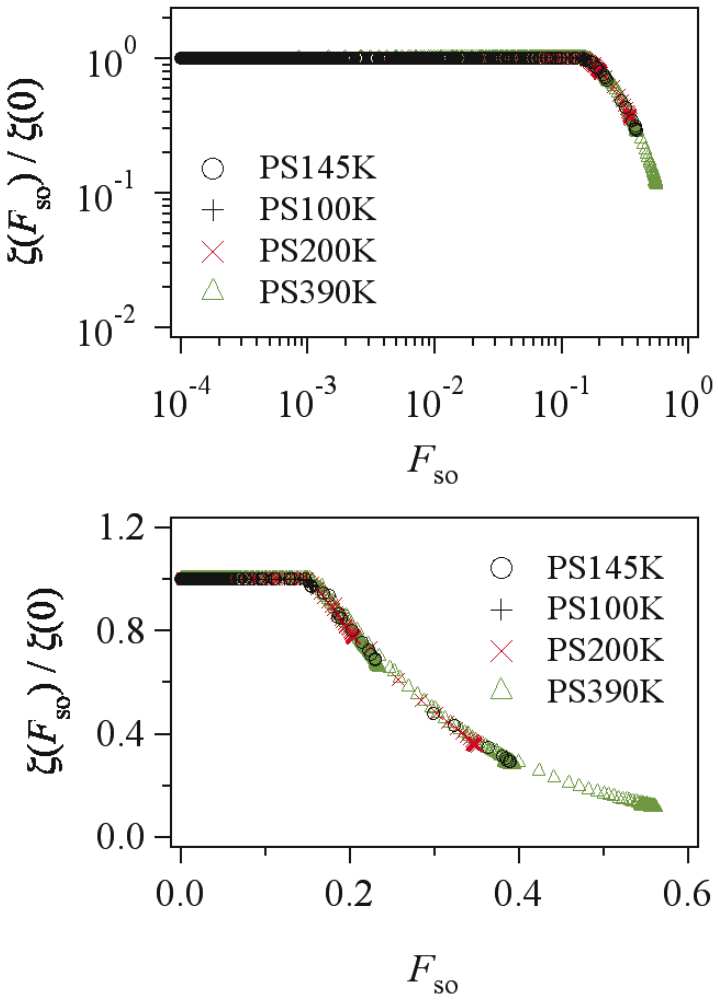

Figure 3-3 Reduction factor of the monomeric friction coefficient ζ plotted against the stretch/orientation parameter F_{so} obtained from the PCN-FENE simulations reported in Figs. 3-1, 3-2, and 3A-1. Scales are logarithmic in the top panel and linear in the bottom panel. Different symbols indicate different PS systems.

Rather good agreement of the simulation results with data (Figs. 3-1 and 3-2) lends support to the molecular mechanism of orientation/stretch-induced reduction of the local friction. The data for PS melts and solutions are consistently described by this idea. However, non-trivial deviations from the data are also noted, for example, for the PS100K melt (top panels of Figs. 3-1 and 3-2). These deviations may be partly attributable to the numerical integration scheme in the simulation that somewhat delays the friction reduction with respect to the orientation/stretch of the subchains and hence overestimates the transient viscosity. It is also possible that the empirical procedure in Chapter 2 giving Eq. 3.10 lacks sufficient precision.

More importantly, the working hypothesis that ζ is dependent only on the stretch/orientation parameter F_{so} ($=\tilde{\lambda}^2\overline{S}$; Eq. 2.1) is open to possible revision. Indeed, ζ could be dependent on the stretch $\tilde{\lambda}$ and the orientation $\overline{S}$ separately, or on a different combination of them. Furthermore, ζ could be of tensorial form under fast flow, as suggested by Uneyama *et al.*[14] Modification along these lines might improve agreement between the simulation and experiments. Nevertheless, the simple idea of the reduction of the scalar ζ due to subchain stretch/orientation led to, in total, a remarkable agreement between the PCN simulation and the data (Figs. 3-1 and 3-2).

3-4-2. Detailed analysis of steady state viscosity

It is also informative to quantify the effect of the friction reduction on various quantities in the PCN-FENE simulation. For this purpose, Figure 3-4 summarizes the viscosity reduction factor $\eta_E/\eta_{E,0}$, the reduced square-stretch of the subchain $\tilde{\lambda}^2$, the average orientation $\overline{S}$, the FENE factor f_{FENE}, the entanglement density reduction Z/Z_0 (appearing in Eq. 3.13), and the $\zeta(F_{so})/\zeta(0)$ ratio, all obtained from the simulation of the PS390K melt in the steady state. These quantities are plotted against the τ_R-based Weissenberg number, $Wi_R\,(=\dot{\varepsilon}\tau_R)$. The solid and dashed curves indicate the results with and without the friction reduction. The $\zeta(F_{so})/\zeta(0)$ ratio starts decreasing with increasing Wi_R above unity (*cf*. bottom panel). This friction reduction affects $\overline{S}$ and f_{FENE} just moderately, but considerably suppresses the subchain stretch, as noted from comparison of the solid and dashed curves in the second top panel. The monotonic thinning of η_E results from a delicate combination of all these effects. (f_{FENE} is slightly larger than unity even at low Wi_R because of the small n_0 value for PS melts; *cf*. Table 3-1.)

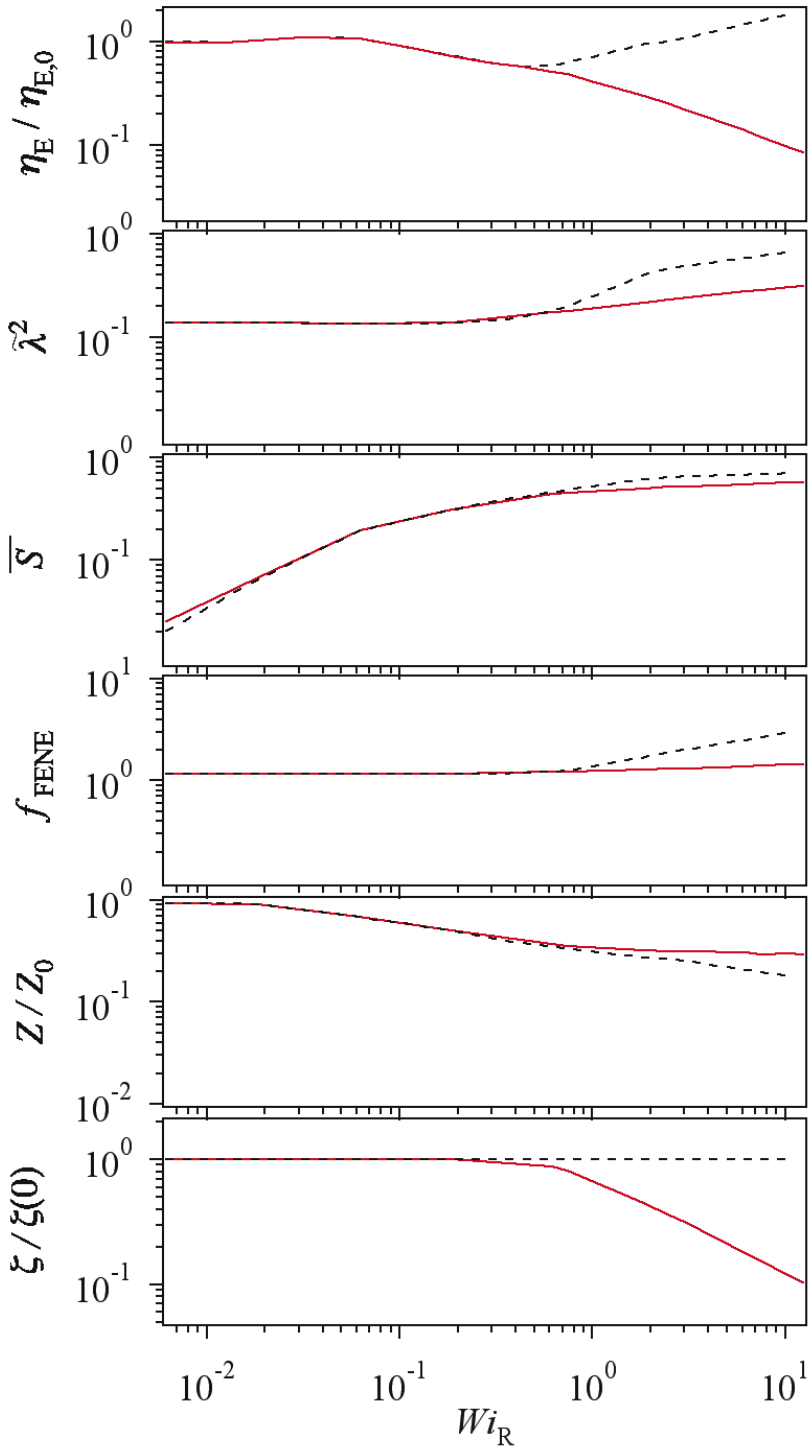

Figure 3-4 Factors representing the viscosity reduction $\eta_E/\eta_{E,0}$, the reduced chain stretch squared $\tilde{\lambda}^2$, the average orientation $\overline{S}$, the FENE factor f_{FENE}, and the local friction reduction $\zeta(F_{so})/\zeta(0)$ obtained from the PCN-FENE simulation for PS390K in the steady state. These factors are plotted against τ_R-based Weissenberg number Wi_R. The simulation results with and without the stretch/orientation-induced reduction of monomeric friction are indicated with the solid and dashed curves, respectively.

3-5. Conclusions

The empirical equation for the friction reduction factor obtained in Chapter 2 was utilized in the primitive chain network (PCN) simulation to examine the elongational behavior of melts and solutions. For PS melts, the simulation indicated significant friction under fast elongational flow, because the entanglement subchains therein are short and approach the full-stretch/full-orientation limit rather easily. Correspondingly, the steady state elongational viscosity η_E of PS melts follows this friction reduction to exhibit the monotonic thinning even at $\dot{\varepsilon} > \tau_R^{-1}$. In contrast, for PS solutions, the simulated η_E exhibited the thinning followed by thickening at $\dot{\varepsilon} > \tau_R^{-1}$ because the average anisotropy $\overline{S}$ was governed by the solvent and remained small thereby not allowing the stretch/orientation parameter F_{so} $(=\tilde{\lambda}^2\overline{S})$ to exceed a threshold value for the friction reduction. These simulated results were in satisfactory agreement with the experiments, which suggested that the difference of η_E of the melts and solution reflects the difference of the local orientational field (largely damped by the solvent in semidilute solutions).

Appendix 3A. Stress growth and relaxation

Figure 3A-1 compares the simulation results with the uniaxial elongational stress growth and relaxation data reported for the PS145K melt[12] and for the PS3.9M 10wt% solution.[9] (The relaxation data are the same as those shown in Chapter 2.) The dashed and solid curves respectively indicate the results of the PCN simulation without and with the orientation/stretch-induced reduction of ζ. The data for $\dot{\varepsilon} > 1/\tau_0^{\mathrm{PCN}}$ were omitted since the simulation has a sound meaning only at $\dot{\varepsilon} < 1/\tau_0^{\mathrm{PCN}}$.

For the PS145K melt (left panel), the simulation with a constant ζ (dashed curves) clearly overestimates the viscosity data. Furthermore, the simulated viscosity at flow cessation, $\eta_{\mathrm{E}}^{\mathrm{cessation}}$, increases with increasing $\dot{\varepsilon}$, whereas the experiments show the opposite trend. In contrast, the simulation results with the friction reduction (solid curves) are much closer to the data and reproduce the decrease of $\eta_{\mathrm{E}}^{\mathrm{cessation}}$ with increasing $\dot{\varepsilon}$ (for $\dot{\varepsilon} > \tau_{\mathrm{R}}^{-1}$), which lends some support to the hypothesis of the friction reduction. For the PS3.9M 10wt% solution (right panel), the friction reduction is negligible in the simulation because the average orientation $\overline{S} = \phi_{\mathrm{P}} S_{\mathrm{P}}$ is small so that the stretch/orientation parameter F_{so} $(= \widetilde{\lambda}^2 \overline{S})$ does not exceed a threshold value for the friction reduction. Such simulation results well mimic the solution data.

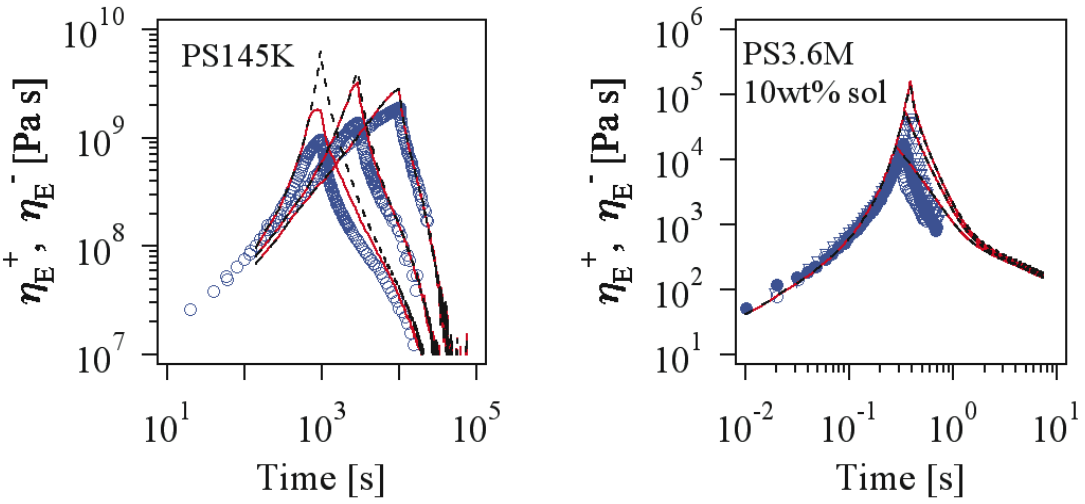

Figure 3A-1 Viscosity growth and relaxation on start-up and cessation of uniaxial elongational flow for PS145K melt[12] at 393 K (left) and PS3.6M 10wt% solution[9] at 294 K (right). Strain rates for PS145K are 0.001, 0.003 and 0.0003 sec^{-1} from left to right and the maximum strain at the flow cessation is 3.0. Strain rate for PS3.6M solution is 11.7 s^{-1} and the maximum strains at the flow cessation are 3.3, 4.0 and 4.6 from left to right. Dashed and solid curves, respectively, indicate the results of PCN-FENE simulation without and with the stretch/orientation-induced reduction of friction. Experimental data are shown with symbols.

Appendix 3B. Nonlinear shear properties

It is important to verify whether or not the friction reduction effect so far examined for elongational flow is also important for shear flow. In the shear case, the orientation of the polymer (subchain), S_P, is defined as the positive difference between the two eigenvalues of the orientation tensor $<\boldsymbol{uu}>$ that correspond to the eigenvectors in the shear plane. Hence:

$$S_P = \sqrt{\{< u_x^2 > - < u_y^2 >\}^2 + 4 < u_x u_y >^2} \qquad (3B.1),$$

where x and y are the shear and gradient directions, respectively. All other equations to be used in the simulation remain the same as in the elongational flow case.

Figure 3B-1 compares the PCN-FENE simulation results with the PS200K-S melt data for the shear viscosity growth function $\eta^+(t,\dot{\gamma})$.[15] The solid curves and plus symbols, respectively, indicate the simulation results with and without the friction reduction. Simulations were made with the parameter values shown in Table 3-1 and covered the whole experimental range of Wi_R (≤ 3.4). At such large $Wi_R \sim 3$, the friction decreases in the elongational flow case to decrease the elongational viscosity (*cf*. middle panels of Figs. 3-1 and 3-2). Conversely, for shear flow, the simulated results with and without friction reduction are indistinguishable and close to the data (*cf*. Fig. 3B-1). In fact, with the shear conditions examined, the stretch/orientation parameter F_{so} remains below the critical value (= 0.14; *cf*. Fig. 3-3) and thus the friction reduction mechanism incorporated in the simulation is essentially ineffective for Wi_R up to 3.4. This result shows that the magnitude of the friction reduction is not uniquely determined by Wi_R, but is also dependent on the type of flow. This result also shows that the previous PCN-FENE simulations for shear flow[6] conducted without accounting for the friction reduction remain valid even after considering this new effect.

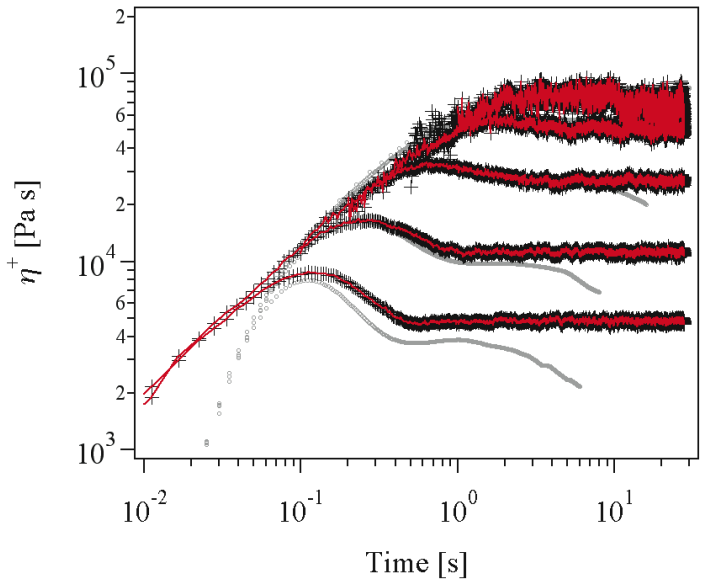

Figure 3B-1 Shear viscosity growth function for PS200K-S[15] at 448 K. The PCN-FENE simulation results with and without the local friction reduction are shown with the solid curves (red) and the plus symbols, respectively. Data from Ref. 15 are shown by (gray) unfilled circles. Shear rates are 30, 10, 3, 1, and 0.3 s^{-1} from bottom to top.

References

1) Y. Masubuchi, J-I. Takimoto, K. Koyama, G Ianniruberto, F. Greco, G Marrucci, Journal of Chemical Physics, 115, 4387 (2001).

2) Y. Masubuchi, K. Furuichi, K. Horio, T. Uneyama, H. Watanabe, G Ianniruberto, F. Greco, G Marrucci, Journal of Chemical Physics, 131, 114906 (2009).

3) T. Yaoita, T. Isaki, Y. Masubuchi, H. Watanabe, G Ianniruberto, G Marrucci, Macromolecules, 44, 9675 (2011).

4) P. Mazur, I. Oppenheim, Physica (Amsterdam) 50, 241 (1970).

5) A. Peterlin, Journal of Chemical Physics, 36, 1799 (1960).

6) T. Yaoita, T. Isaki, Y. Masubuchi, H. Watanabe, G Ianniruberto, F. Greco, G Marrucci, Journal of Chemical Physics, 128, 154901 (2008).

7) Y. Masubuchi, G Ianniruberto, F. Greco, G Marrucci, Journal of Non-Crystalline Solids, 352, 5001 (2006).

8) H. Janeschitz-Kriegl, *Polymer melt rheology and flow birefringence*, (Springer, Berlin, 1983).

9) P. K. Bhattacharjee, D. A. Nguyen, G H. McKinley, T. Sridhar, Journal of Rheology, 47, 269 (2003).

10) A. Bach, K. Almdal, H. K. Rasmussen, O. Hassager, Macromolecules, 36, 5174 (2003).

11) M. H. Wagner, S. Kheirandish, O. Hassager, Journal of Rheology, 49, 1317 (2005).

12) J. K. Nielsen, H. K. Rasmussen, O. Hassager, Journal of Rheology, 52, 885 (2008).

13) M. Rubinstein, R. Colby, *Polymer Physics*, Oxford University Press Inc, Oxford (2003).

14) T. Uneyama, K. Horio, H. Watanabe, Physical Review E, 83, 001800 (2011).

15) T. Schweizer, J. van Meerveld, H. C. Öttinger, Journal of Rheology, 48, 1345 (2004).

CHAPTER 4

Uniaxial elongational viscoelastic behavior investigated through a single-chain model

4-1. Introduction

In Chapter 3, the stretch/orientation-induced friction, $\zeta(F_{so})$, was implemented into the PCN simulation[1),2)] for the test on uniaxial elongational viscosity for PS melts[3),4)] and solutions.[5)] That simulation semi-quantitatively captured the experimental data both for melts and solutions, suggesting that the stretch/orientation-induced friction reduction is one possible origin of the failure of universality in the elongational behavior of the melts and solutions. However, it is necessary to make further tests for several factors, for example, possible artificial coupling between the formulation of the friction reduction and the multi-chain modeling in the simulation.

Thus, this Chapter attempts to test the friction reduction without utilizing the simulation. For this purpose, the friction reduction is incorporated in a simplified version of the molecular model (toy model) proposed by Mead, Larson, and Doi (MLD).[6)] This toy model does not give very accurate description of the viscoelastic functions because of its lack of relaxation mode distribution, but it still reproduces the universality of the viscoelastic functions under shear. Incorporation of the friction reduction resulted in breakdown of the universality under elongational flow, as expected. Details of the model and its prediction are described below.

4-2. Model

In the MLD toy model,[6] the entangled polymer chain is regarded as a dumbbell that reptates in a tube. The model considers conventional relaxation mechanisms such as reptation, TCR, CLF, chain stretch, and CCR, though CLF is just accounted by rescaling the reptation time. The times required for the dumbbell contraction (corresponding to the Rouse time) and the reptation in the liner regime (at equilibrium) are denoted by τ_R and τ_d, respectively. Finite extensible nonlinear elasticity (FENE) was later incorporated into the MLD toy model by Pattamaprom and Larson,[7] and Ye *et al.*[8] With the decoupling approximation proposed by Pearson *et al.*,[9] stress tensor $\boldsymbol{\sigma}$ with FENE in the model[7),8)] is expressed as

$$\boldsymbol{\sigma} = 5G_N^0 f_{FENE} \lambda^2(t)\mathbf{S}(t) \tag{4.1},$$

where G_N^0 is the entanglement plateau modulus, λ is the chain stretch ratio, $\mathbf{S}$ is the orientation tensor, and f_{FENE} is the FENE factor. The model examined in this Chapter adopts the simplest form of f_{FENE} (*cf.* Eq. 3.6),[10]

$$f_{FENE} = \frac{1}{1-\tilde{\lambda}^2} \qquad \text{with} \qquad \tilde{\lambda} = \lambda / \lambda_{max} \tag{4.2},$$

where λ_{max} is the maximum stretch ratio of the dumbbell. λ_{max} is a constant in the MLD toy model, whereas λ_{max} increases on loss of entanglements in the PCN multi-chain model[2] as described in Chapter 3.

The time evolution of $\mathbf{S}$ is described by[6),7),8)]

$$\mathbf{S}(t) = \int_{-\infty}^{t} \frac{dt'}{\tau(t')} \exp\left[-\int_{t'}^{t} \frac{dt''}{\tau(t'')} \right] \mathbf{Q}\left[\mathbf{E}(t,t')\right] \tag{4.3},$$

where $\mathbf{Q}\left[\mathbf{E}(t,t')\right]$ is the universal deformation tensor and is calculated by the Curie's formula[11] with the independent alignment approximation that assumes respective

entanglement subchains to be oriented independently after contraction (and keep the orientation before the contraction). This approximation gives the stress decay by a factor of 3/5 due to the fluctuation of the entanglement points, which leads to a prefactor of "5" in Eq. 4.1.

τ appearing in Eq. 4.3 is the effective relaxation time specified by[7)]

$$\frac{1}{\tau} = \frac{1}{\lambda^2 \tau_d} + \frac{1}{\lambda}\left(\boldsymbol{\kappa} : \mathbf{S} - \frac{\dot{\lambda}}{\lambda} + \frac{1}{\lambda^2 \tau_d} \right) \tag{4.4}.$$

The first term on the RHS represents the relaxation due to reptation along the tube stretched by the factor of λ. The second term shows the effect of thermal and convective constraint release (TCR and CCR) on τ, with the prefactor before the parenthesis, λ^{-1}, serving as the switching function.[6),7),8)] The first term in the parenthesis indicates the center of mass convection due to the flow specified by the strain rate tensor $\boldsymbol{\kappa}$. The second term indicates an effect of contraction on the dumbbell (chain) disorientation. The third term indicates an effect of TCR.

The stretch ratio λ involved in Eqs. 4.1, 4.2 and 4.4 obeys the following time evolution equation,[7)]

$$\dot{\lambda} = \lambda(\boldsymbol{\kappa} : \mathbf{S}) - \frac{f_{\mathrm{FENE}}}{\tau_R}(\lambda - 1) - \frac{1}{2}\left(\boldsymbol{\kappa} : \mathbf{S} - \frac{\dot{\lambda}}{\lambda} + \frac{1}{\lambda^2 \tau_d} \right)(\lambda - 1) \tag{4.5}.$$

The first term on the RHS of Eq. 4.5 indicates the stretch due to flow, and the second term shows the release of stretch on contraction of the dumbbell affected by the FENE spring. The TCR/CCR effects on λ are cast in the third term, as similar to the description in Eq. 4.4.

The stretch/orientation-induced friction reduction is incorporated into the model. This reduction should affect both contraction and reptation times, τ_R' and τ_d'.

Specifically, τ'_{R} and τ'_{d} should be proportional to the friction ζ of the dumbbell bead (chain segment). Thus, the ratio r of τ'_{R} and/or τ'_{d} under elongation to τ_{R} and/or τ_{d} at equilibrium is assumed to be uniquely determined by a single parameter, the stretch/orientation factor $F_{\mathrm{so}} = \tilde{\lambda}^2 \bar{S}$ (*cf.* Eq. 2.1) as

$$\frac{\tau'_{\mathrm{R}}(F_{\mathrm{so}})}{\tau_{\mathrm{R}}} = \frac{\tau'_{\mathrm{d}}(F_{\mathrm{so}})}{\tau_{\mathrm{d}}} = r(F_{\mathrm{so}}) \qquad (4.6a),$$

with

$$r(F_{\mathrm{so}}) \equiv \frac{\zeta(F_{\mathrm{so}})}{\zeta(0)} = f_{\mathrm{FENE}} \frac{1}{(1+\beta)^{\gamma}} \left\{ \beta + \frac{1 - \tanh \alpha (F_{\mathrm{so}} f_{\mathrm{FENE}} - F^*_{\mathrm{so}})}{2} \right\} \qquad (4.6b).$$

Equation 4.6b is identical to the empirical equation described in Chapter 2 (*cf.* Eq. 2.8), and the parameters are $\alpha = 20$, $\beta = 5 \mathrm{x} 10^{-9}$, $\gamma = 0.15$ and $F^*_{\mathrm{so}} = 0.14$. The average orientation $\bar{S}$ is calculated as $\bar{S} = \phi_{\mathrm{p}}(S_{zz} - S_{xx})$, where ϕ_{p} is the polymer volume fraction and S_{zz} and S_{xx} are the components of orientation tensor (with z and x specifying the directions parallel and perpendicular to the elongation). From Eq. 4.6, Equations 4.4 and 4.5 are rewritten as

$$\frac{1}{\tau} = \frac{1}{\lambda^2 r(F_{\mathrm{so}}) \tau_{\mathrm{d}}} + \frac{1}{\lambda} \left(\boldsymbol{\kappa} : \mathbf{S} - \frac{\dot{\lambda}}{\lambda} + \frac{1}{\lambda^2 r(F_{\mathrm{so}}) \tau_{\mathrm{d}}} \right) \qquad (4.7),$$

$$\dot{\lambda} = \lambda (\boldsymbol{\kappa} : \mathbf{S}) - \frac{f_{\mathrm{FENE}}}{\tau_{\mathrm{R}} r(F_{\mathrm{so}})} (\lambda - 1) - \frac{1}{2} \left(\boldsymbol{\kappa} : \mathbf{S} - \frac{\dot{\lambda}}{\lambda} + \frac{1}{\lambda^2 \tau_{\mathrm{d}} r(F_{\mathrm{so}})} \right) (\lambda - 1) \qquad (4.8).$$

The time evolution of the modified MLD toy model is fully specified by Eqs. 4.3, 4.7 and 4.8, and the stress is calculated from Eq. 4.1. (FENE does not affect the reptation time so that the time evolution of τ is modified only for the friction reduction, as shown in Eq. 4.7.)

The model parameters (G^0_{N}, $\lambda_{\max}$, τ_{d} and τ_{R}) are evaluated from the linear

viscoelastic data of PS melts[3),4)] and solution,[5)] as explained in Appendix 4A. The parameters for the PS melts/solution examined in this study are summarized in Table 4-1.

Table 4-1 Model parameters for the PS melts and solution.

Sample	M /kg mol^{-1}	c /kg m^{-3}	G_N^0 /Pa	λ_{max}	τ_d /s	τ_R /s	T /K
PS100K**	1.0x10^2	9.7x10^2	1.6x10^5	4.8	9.4x10	9.9	403
PS200K*	2.0x10^2				9.6x10^2	3.8x10	
PS390K*	3.9x10^2				1.1x10^4	1.4x10^2	
3.9M 10wt%***	3.9x10^3	9.7x10	1.3x10^3	1.4x10	1.2x10	1.1x10^{-1}	294

The experimental data were obtained from * ref.3, ** ref.4 and *** ref.5.

4-3. Results and discussion

4-3-1. Overview of uniaxial elongational behavior

To understand the relaxation dynamics under uniaxial elongational flow, calculations by the MLD toy model were conducted with and without the stretch/orientation-induced friction reduction. The top and bottom panels of Fig. 4-1 show the elongational viscosity growth function $\eta_E^+(t,\dot{\varepsilon})$ and the steady state elongational viscosity $\eta_E(\dot{\varepsilon})$ reported for the PS solution.[5)] In the bottom panel, $\eta_E(\dot{\varepsilon})$ is plotted against the Weissenberg number defined with respect to the Rouse relaxation time at equilibrium, $Wi_R = \dot{\varepsilon}\tau_R$. For this solution, the average orientation $\overline{S}$ never exceeds 0.1 because of the solvent (90 % in the system) so that the friction in the model stays at its equilibrium value $\zeta(0)$ even at the highest deformation rate. Consequently, the model is essentially the same with that used by Ye *et al.*[8)] The calculation results (dotted curves) are not in quantitative

agreement with the data (symbols) for $\eta_E^+(t,\dot{\varepsilon})$ partly due to the uncertainty of the model parameters explained in Appendix 4A. However, the basic feature of the experimental data, upturn of $\eta_E(\dot{\varepsilon})$ for $Wi_R \geq 1$, is reasonably captured, as reported earlier.[8)]

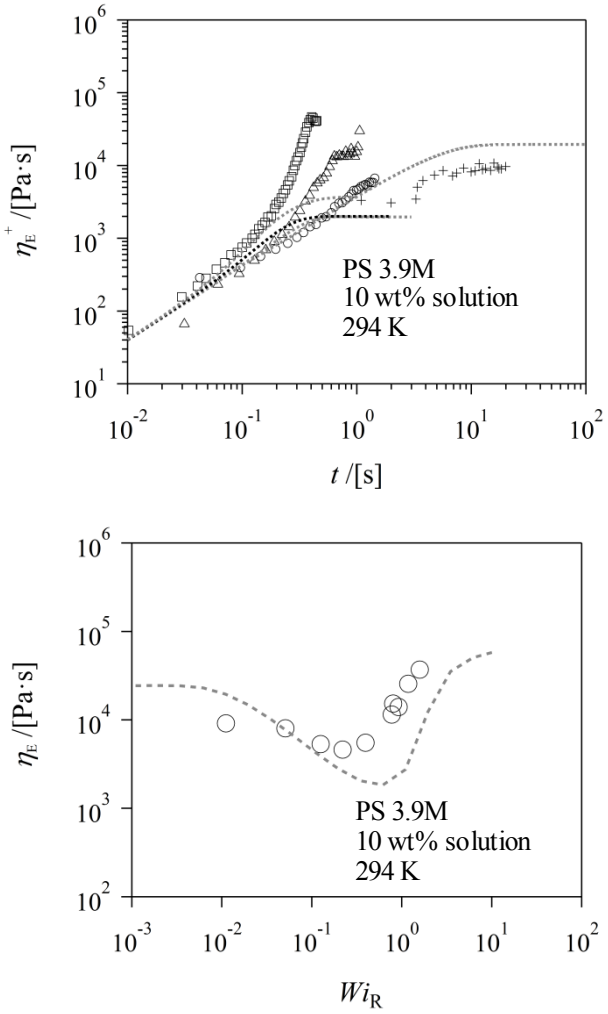

Figure 4-1 Elongational viscosity growth function (top panel) and steady state elongational viscosity (bottom panel) of the PS solution[5)] (M_w = 3.9x10^6 kg/mol, 10 wt%, 294 K). Symbols indicate the experimental data and dotted curves are the MLD toy model calculations. The strain rates are $\dot{\varepsilon} = 0.1$, 3.5, 7.3, and 11.7 s^{-1} in the top panel, where the calculation for 7.3 s^{-1} is plotted in black for clarity. In the bottom panel, the steady state elongational viscosity is plotted against the τ_R-based Weissenberg number Wi_R.

Figures 4-2 and 4-3, respectively, show $\eta_E^+(t,\dot{\varepsilon})$ and $\eta_E(\dot{\varepsilon})$ for the PS melts.[3),4)] The symbols indicate the literature data, and the solid and dotted curves, the MLD toy model calculations with and without the friction reduction. For the calculation without the friction reduction, $r(F_{so})$ was artificially fixed at unity (*i.e.*, Eq. 4.6b was not utilized). For rather slow flow at $Wi_R < 1$, the calculated results with and without the friction reduction are indistinguishable (because F_{so} does not exceed the threshold and $r(F_{so})$ given by Eq. 4.6b is very close to unity) and close to the data. For faster flow ($Wi_R > 1$), the calculated $\eta_E(\dot{\varepsilon})$ shows the upturn (as also noted in the earlier studies[8)]) if $r(F_{so})$ is artificially fixed at unity; see the dotted curves in Fig. 4-3. In contrast, this upturn essentially vanishes if $r(F_{so})$ given by Eq. 4.6b is utilized; see the solid curves. The corresponding difference is noted in Fig. 4-2 for $\eta_E^+(t,\dot{\varepsilon})$ at $Wi_R > 1$. Clearly, the calculation without the friction reduction significantly overestimates the $\eta_E(\dot{\varepsilon})$ and $\eta_E^+(t,\dot{\varepsilon})$ data at $Wi_R > 1$ where the $\eta_E(\dot{\varepsilon})$ data exhibit monotonic decrease with Wi_R. On the other hand, the calculation with this reduction reasonably describes the data within a factor $\sim$ 2, although quantitative agreement cannot be obtained/expected because of the toy nature of the utilized model. This result suggests that the stretch/orientation-induced friction reduction coexists with conventional relaxation mechanisms such as reptation, TCR, CLF, chain stretch, CCR, lending support to the concept of the friction reduction.

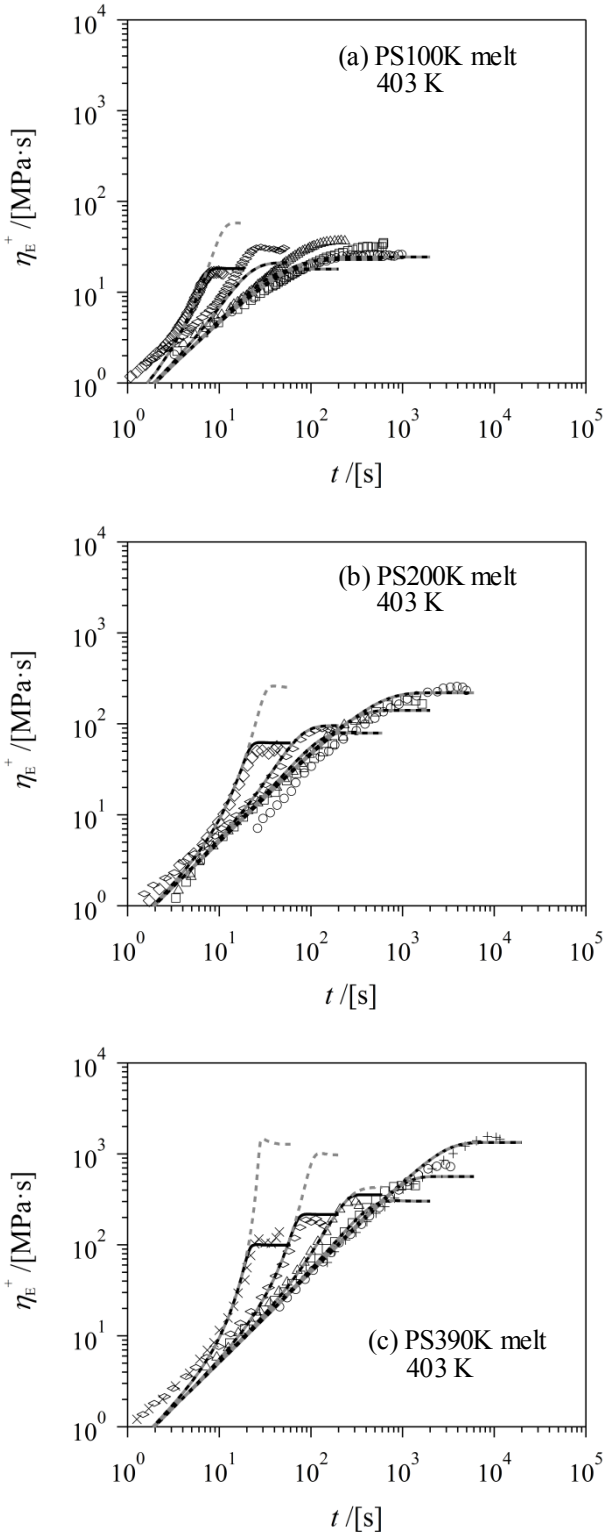

Figure 4-2 Elongational viscosity growth function of the PS melts with the molecular weight of (a) 100K,[4] (b) 200K,[3] and (c) 390K[3] at 403 K. Symbols indicate the data. The solid and dotted curves are MLD toy model calculations with and without the friction reduction, respectively. The strain rates are: (a) 0.003, 0.01, 0.03, 0.1, and 0.3 s^{-1}, (b) 0.001, 0.003, 0.01, 0.03, and 0.1 s^{-1} and (c) 0.0003, 0.001, 0.003, 0.01, 0.03, and 0.1 s^{-1}, respectively.

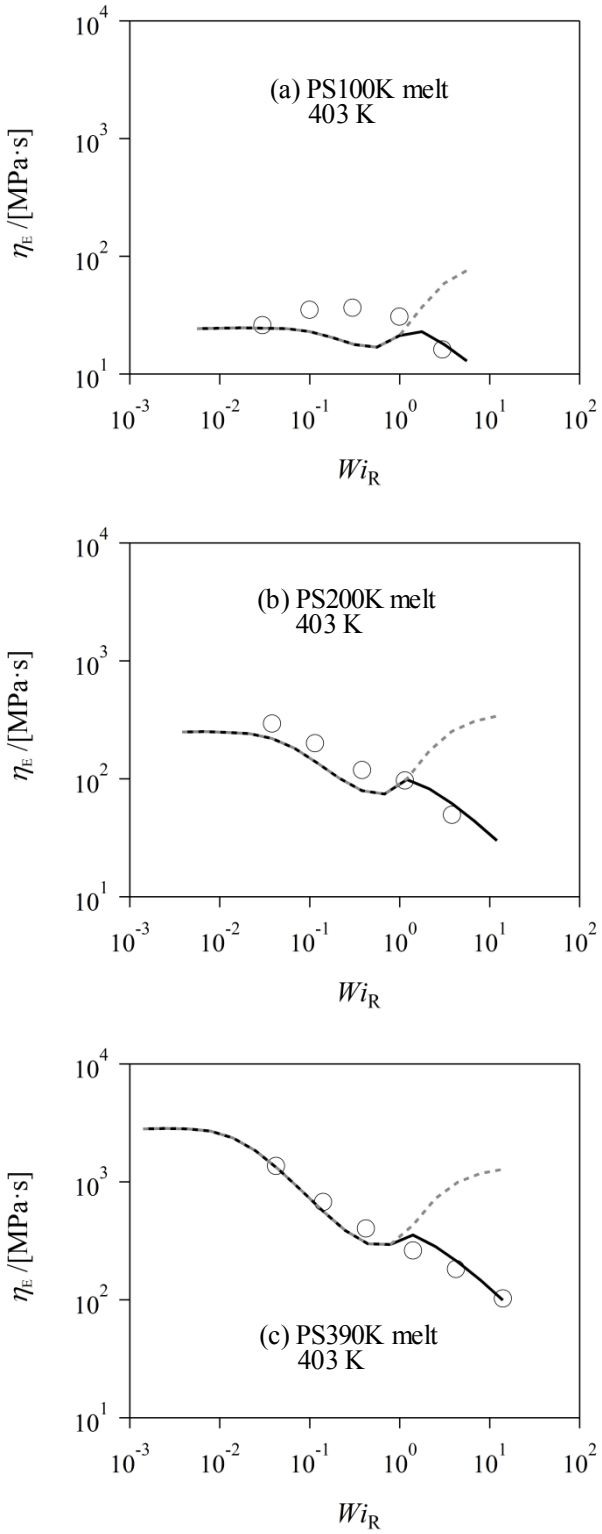

Figure 4-3 Steady state elongational viscosity of the PS melts examined in Fig. 4-2 plotted against the τ_R-based Weissenberg number Wi_R. Symbols indicate the data.[3),4)] The solid and dotted curves are MLD toy model calculations with and without the friction reduction, respectively.

4-3-2. Decoupling analysis of steady state viscosity

Figure 4-4 shows plots of the orientation $\overline{S}$, normalized stretch $\widetilde{\lambda}$, and the FENE factor f_{FENE} calculated for PS390K melt in the steady state against Wi_{R}. For comparison, the steady state viscosity $\eta_{\mathrm{E}}(\dot{\varepsilon})$ and the friction reduction ratio r are also shown. Comparison of the calculations with and without the friction reduction (solid and dotted curves) clearly indicates that the reduction hardly affects $\overline{S}$ but suppresses the increase of $\widetilde{\lambda}$ and f_{FENE}, thereby suppressing the increase of the stress and the upturn of $\eta_{\mathrm{E}}(\dot{\varepsilon})$. This feature is similar to that observed for the PCN simulation in Chapter 3, but the increase of f_{FENE} is more significantly suppressed in the MLD toy model calculation. This difference of f_{FENE} can be related to the CCR-induced decrease of the entanglement number that occurs in the PCN simulation but not in the toy model, the latter regarding the chain as the dumbbell.

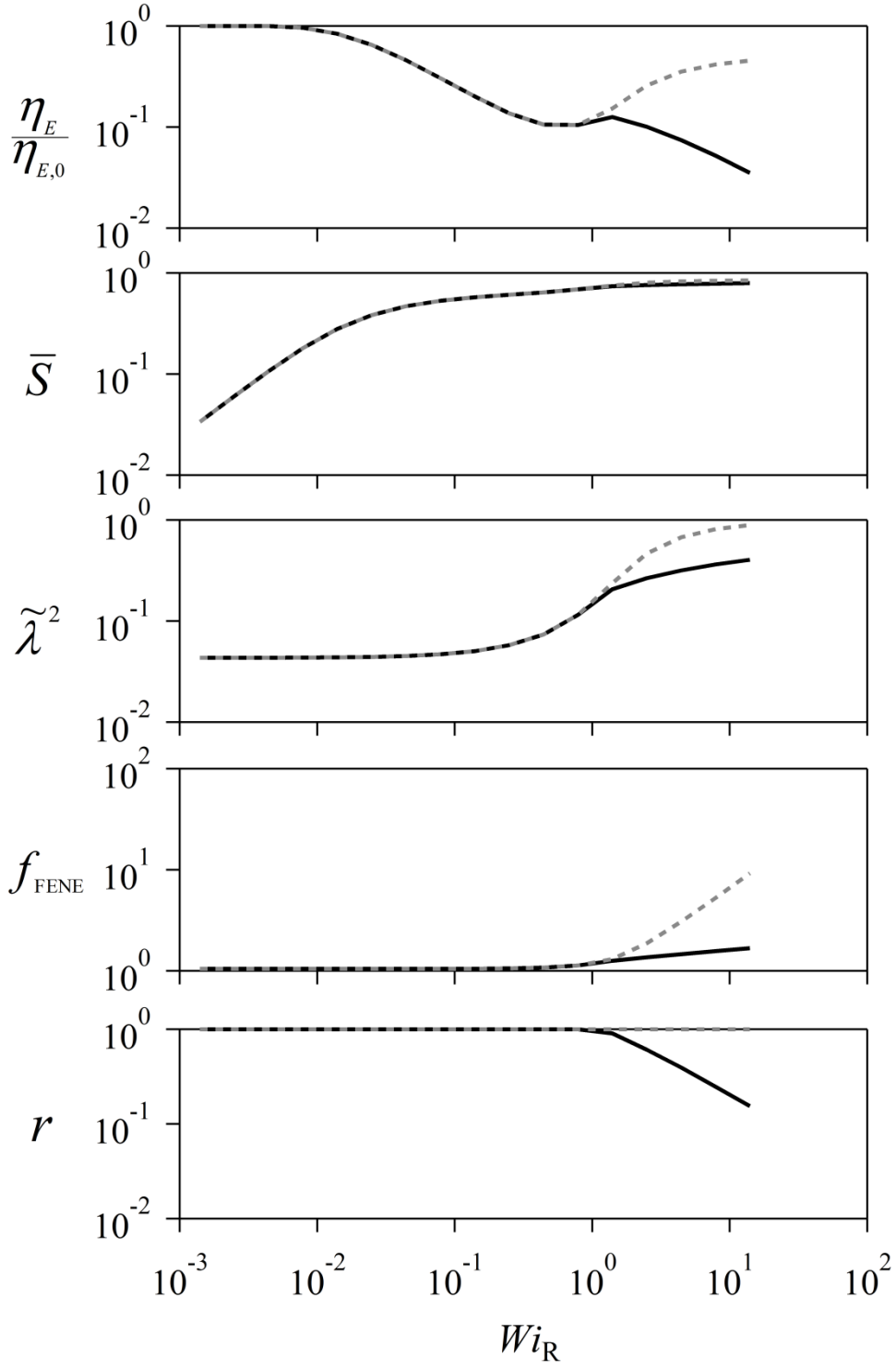

Figure 4-4 Steady-state viscosity η_{E} (normalized by the equilibrium value $\eta_{\mathrm{E},0}$), average orientation $\bar{S}$, normalized stretch ratio $\tilde{\lambda}$ (squared), FENE factor f_{FENE}, and friction reduction ratio r calculated for PS390K melt. These parameters, calculated with and without the friction reduction (solid and dotted curves), are plotted against τ_{R}-based Weissenberg number Wi_{R}.

4-4. Conclusions

The stretch/orientation-induced reduction of monomeric friction was implemented into the MLD toy model, and the uniaxial elongational behavior of a PS solution and melts were calculated. For the PS solution, the calculation with and without the friction reduction gave indistinguishable results (because the solvent therein prevents the friction reduction) that agreed with the data within a factor ~2. On the other hand, for the PS melts, the calculation with the friction reduction described the data again within a factor ~2, whereas lack of this reduction led to much larger deviation (including divergence of the calculated viscosity at high strain rates). These results are consistent with those of the PCN simulation described in Chapter 3, lending support to the idea of stretch/orientation-induced friction reduction irrespective of the method/model of calculation.

Appendix 4A. Model parameters

The material parameters, τ_d, G_N^0, τ_R, and λ_{max} shown in Table 4-1 were evaluated from the linear viscoelastic data of the PS melts[3),4)] and solution,[5)] as explained below.

The longest relaxation time τ_d was evaluated from the zero-shear viscosity η_0 and the steady state compliance J_e^0 as

$$\tau_d = \eta_0 J_e^0 \tag{4A.1}.$$

G_N^0 and τ_R are coupled with each other through the entanglement molecular weight M_e. For a given M_e, they can be written, within the context of the tube model, as[12),13)]

$$G_N^0 = 0.8\frac{cRT}{M_e} \tag{4A.2},$$

$$\tau_R = \frac{12M\eta_0}{\pi^2 cRT}\left(\frac{1.5M_e}{M}\right)^{2.4} \tag{4A.3}.$$

Here, R, T, c and M are the gas constant, absolute temperature, and the mass concentration, and molecular weight of polymer, respectively. For evaluation of M_e, the following iteration procedure was employed. First, a presumed value of M_e is adopted to calculate the Rouse contribution to the storage modulus, G'_R, and subtracted G'_R from the experimental G' to obtain the entanglement contribution $G'_e = G' - G'_R$. Then, G_N^0 is evaluated as the plateau value of G'_e at sufficiently high frequencies ($\omega >> \tau_R^{-1}$). From this G_N^0 value, M_e is re-calculated with Eq. 4A.2 and compared with the initial value. This procedure is iterated until the value of M_e converged.

Figure 4A-1 shows the Rouse and the entanglement contributions to the experimental data obtained after this convergence. For the solution (bottom panel), G'_e

did not show the full entanglement plateau because of the lack of the data at sufficiently high frequencies. Consequently, the parameters for the solution involved some uncertainties.

Finally, the maximum stretch ratio λ_{max} was calculated from M_e as

$$\lambda_{max} = \sqrt{\frac{M_e}{M_K}} \qquad \text{(4A.4).}$$

Here, M_K is the molecular weight of the Kuhn segment and assumed to be 720.[14)]

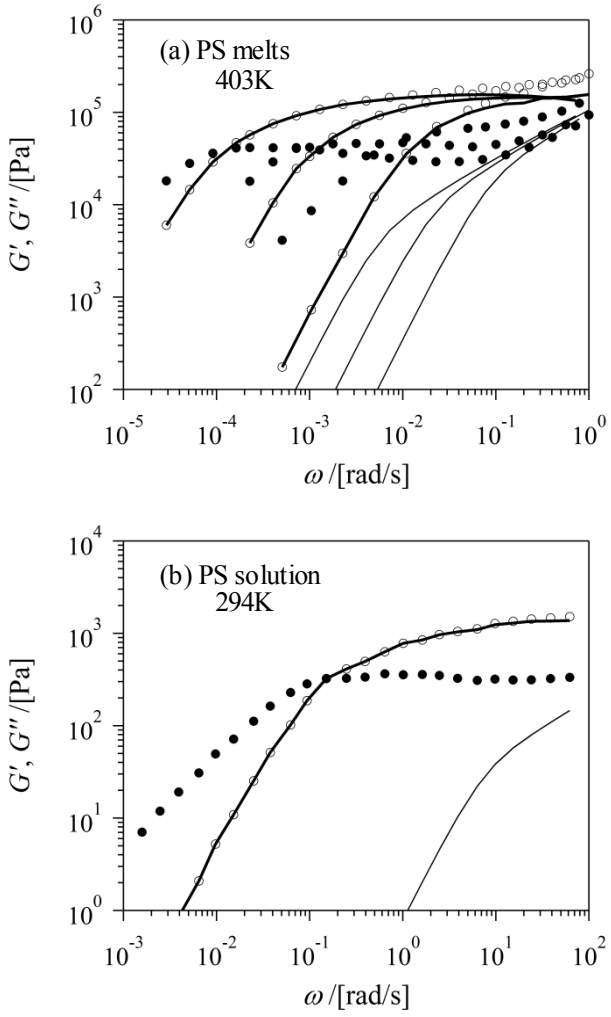

Figure 4A-1 Linear viscoelastic data for the examined PS melts[3),4)] (top panel) and solution[5)] (bottom panel). Unfilled and filled circles indicate experimental storage and loss modulus, respectively. Thick and thin curves, respectively, show the entanglement and Rouse contributions to the storage modulus.

References

1) Y. Masubuchi, J-I. Takimoto, K. Koyama, G Ianniruberto, F. Greco, G Marrucci, Journal of Chemical Physics, 115, 4387 (2001).

2) T. Yaoita, T. Isaki, Y. Masubuchi, H. Watanabe, G Ianniruberto, G Marrucci, Macromolecules, 44, 9675 (2011).

3) A. Bach, K. Almdal, H. K. Rasmussen, O. Hassager, Macromolecules, 36, 5174 (2003).

4) M. H. Wagner, S. Kheirandish, O. Hassager, Journal of Rheology, 49, 1317 (2005).

5) P. K. Bhattacharjee, D. A. Nguyen, G H. McKinley, T. Sridhar, Journal of Rheology, 47, 269 (2003).

6) D. W. Mead, R. G Larson, M. Doi, Macromolecules, 31, 7895 (1998).

7) C. Pattamaprom, R. G Larson, Macromolecules 34, 5229 (2001).

8) X. Ye, R. G Larson, C. Pattamaprom, T. Sridhar, Journal of Rheology, 47, 443 (2003).

9) D. S. Pearson, A. D. Kiss, L. J. Fetters, M. Doi., Journal of Rheology, 33, 517 (1989).

10) A. Peterlin, Journal of Chemical Physics, 36, 1799 (1960).

11) P. K. Curie, Proceeding of 8th International Rheology Conference, Naples, Italy (1980).

12) M. Doi, S. F. Edwards, *"The theory of polymer dynamics"*, Oxford University Press Inc, Clarendon (1986).

13) K. Osaki, T. Inoue, T. Uematsu, Y. Yamashita, Journal Polymer Science Polymer Physics Edition, 39, 1704 (2001).

14) M. Rubinstein, R. Colby, *Polymer Physics*, Oxford University Press Inc, Oxford (2003).

CHAPTER 5

Nonlinear stress relaxation in coarse-grained molecular dynamics simulations

5-1. Introduction

In the previous Chapters, the stretch/orientation-induced friction reduction has been examined as a possible factor leading to the lack of universality observed for PS melts[1),2)] and solutions[3)] under fast elongational flow. In Chapter 2, an empirical equation was obtained for the friction reduction factor $\zeta(F_{so})/\zeta(0)$. In Chapters 3 and 4, this factor was implemented to molecular models to calculate the elongational viscosity. The models succeeded to reproduce the difference between melts and solutions, suggesting that the friction reduction is a possible mechanism of the lack of universality. However, experimental data for determination of the $\zeta(F_{so})/\zeta(0)$ factor are just rarely available due to experimental difficulties. Indeed, such data are available only for one specific PS sample[4)] and a few PS solutions.[3)] Experiments in shear can be more easily conducted, but the acceleration attributable to the friction reduction has not been observed (because the stretch ratio $\tilde{\lambda}$ never becomes sufficiently large under the shear conditions so far examined). Thus, further investigation is desired to clarify the origin of the acceleration of stress relaxation after cessation of elongational flow.

For this purpose, this Chapter conducts the Kremer-Grest[5)] (KG) simulations utilizing coarse-grained bead-spring chains to examine the friction reduction. In the simulation, the intrinsic bead friction (Γ shown later in Eq. 5.3) is kept constant and the uniaxial elongational flow is applied to the system containing many chains. From the stress relaxation after cessation of the flow, the "effective" friction reduction factor

$\zeta(F_{so})/\zeta(0)$ is extracted. Details of the simulation and the friction reduction thus observed are described below.

5-2. Model

In the bead-spring model of Kremer and Grest,[5] polymer chains are consisted of beads being connected through the finite extension nonlinear elastic (FENE) potential $U^{\mathrm{FENE}}(r)$:

$$U^{\mathrm{FENE}}(r)=\begin{cases}-\frac{1}{2}k_s R_0^2 \ln\left(1-\left(\frac{r}{R_0}\right)^2\right), & (r<R_0),\\ \infty, & (r\geq R_0).\end{cases} \tag{5.1}$$

Here, k_s is the spring constant and R_0 is the maximum extension of the spring. All beads in the system interact with each other through truncated-shifted Lennard-Jones (LJ) potential $U^{\mathrm{LJ}}(r)$:

$$U^{\mathrm{LJ}}(r)=\begin{cases}4\varepsilon\left[\left\{\left(\frac{\sigma}{r}\right)^{12}-\left(\frac{\sigma}{r}\right)^{6}\right\}-\left\{\left(\frac{\sigma}{r^{\mathrm{cut}}}\right)^{12}-\left(\frac{\sigma}{r^{\mathrm{cut}}}\right)^{6}\right\}\right], & (r\leq r^{\mathrm{cut}}),\\ 0, & (r>r^{\mathrm{cut}}).\end{cases} \tag{5.2}$$

Here ε is the unit of the energy, σ is the unit of length, and r^{cut} is the cutoff distance of the LJ potential. The time evolution of beads at position $\mathbf{r}_i$ is described by the following Langevin equation,

$$m\frac{d^2\mathbf{r}_i}{dt^2}=-\frac{\partial U}{\partial \mathbf{r}_i}-\Gamma\frac{d\mathbf{r}_i}{dt}+\mathbf{W}_i(t) \tag{5.3},$$

where m is the mass of the bead, U is the total potential energy of the system, Γ is the

intrinsic friction constant. $\mathbf{W}_i(t)$ is a Gaussian random white noise characterized by[6)]

$$\left\langle \mathbf{W}_i(t) \cdot \mathbf{W}_j(t') \right\rangle = 2k_B T m \Gamma \delta_{ij} \delta(t-t') \mathbf{I}. \quad (5.4),$$

where k_B is the Boltzman constant and $\mathbf{I}$ is the unit tensor. The stress tensor $\boldsymbol{\sigma}$ in the Kremer-Grest model is written as

$$\boldsymbol{\sigma} = \sum_i \left(\frac{\mathbf{p}_i \mathbf{p}_i}{m} + \mathbf{r}_i \mathbf{F}_i \right) / V_{cell} \quad (5.5),$$

where the first term on the RHS represents the contribution from kinetic part with $\mathbf{p}_i = m\mathbf{r}_i$ being a momentum of i-th bead. The second term indicates the contribution from the potential force between the beads, $\mathbf{F}_i = -\frac{\partial U}{\partial \mathbf{r}_i}$.

5-3. Simulations

The KG simulation was made for a linear polymer melt system having the bead number per chain N=40 and the chain number in the periodic boundary box M=30. No entanglement emerges for this N value.[5)] The system size proved sufficiently large to correctly reproduce the relaxation at equilibrium.[7)] The number density of beads and the parameters of the potential (Eq. 5.2) were set to follow the standard model.[5)] After equilibration, the simulation box was uniaxially elongated up to the Hencky strain of 2.0 at a constant stretching rate ranging from $0.05\sigma/\tau_0$ to $0.5\sigma/\tau_0$ (where σ and τ_0 are the standard Lennard-Jones units for length and time). Then, the elongation was stopped and the stress relaxation was detected. Twenty runs with different initial configurations were made for each stretch rate so as to obtain acceptable statistics.

The simulations were performed by using the software COGNAC[8)] (ver 7.1 included in OCTA 2010 package). The following parameter set was used: k_s=30ε/σ^2, R_0=1.5σ, and

Γ=0.5τ^{-1}, where τ is the unit time given by $\sigma(m/\varepsilon)^{1/2}$. The interval of one time step was 0.012τ. r^{cut} between connected beads was set to $2^{1/6}\sigma$ and that between unconnected beads was set to 2.5σ. The unit of temperature was T_0=k_B/ε. The bead number density per unit volume was set to 0.85.

5-4. Results and discussion

5-4-1. Acceleration of stress relaxation in simulation

Figure 5-1 shows the stress relaxation after cessation of elongation obtained from the KG simulation. The stress at time t after cessation of elongation, $\sigma_E^-(t)$, is normalized by the stress, $\sigma_E^-(\tau_0)$, at a reference time τ_0 so as to eliminate possible contributions from non-bond interactions that relax within τ_0.[9] The relaxation is clearly accelerated with increasing rate of the pre-elongation (*cf*. Fig. 5-1(a)), despite the intrinsic friction of the bead, Γ appearing in Eq. 5.3, was kept constant. In Fig. 5-1(b), the $\sigma_E^-(t)/\sigma_E^-(\tau_0)$ ratio is reduced by an adequately chosen damping factor h_E. Clearly, the reduced ratios collapse on a master curve at long t and the time-rate separability[10] holds, as similar to the experiments (*cf*. Fig. 2-6(a)). Thus, the simulation shows the acceleration only at short times, indicating that the acceleration occurs only for higher relaxation modes.

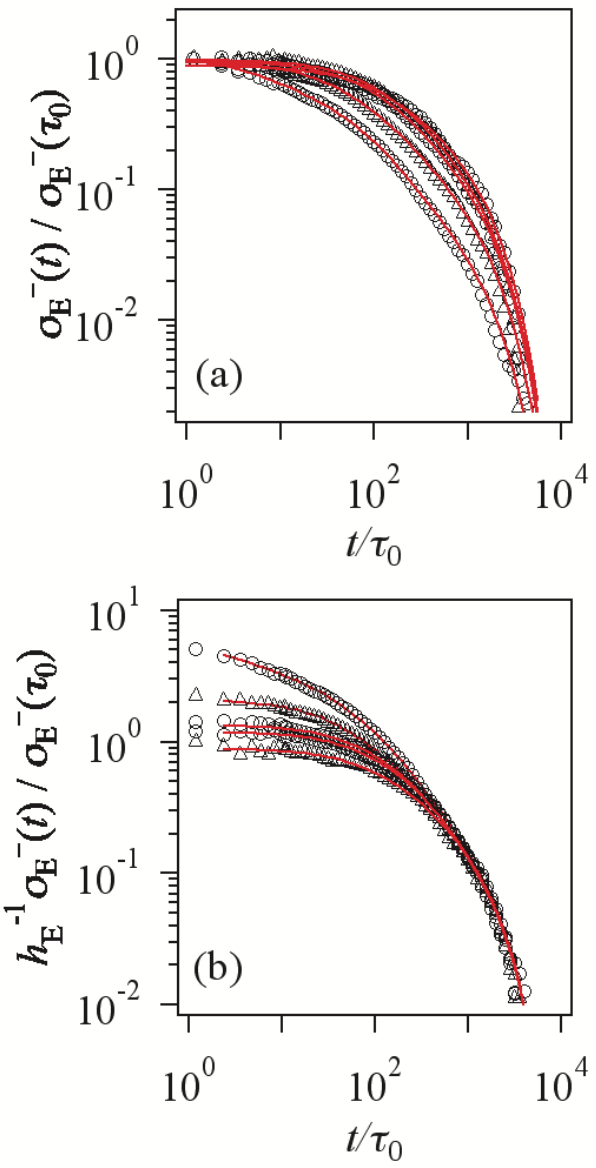

Figure 5-1 Stress decay after cessation of elongational stretch (top panel, (a)) and test of time-rate factorability at long t (bottom panel, (b)). The stretch velocities are 0.05, 0.075, 0.1, 0.2 and 0.5 (σ/τ_0) from top to bottom in (a) and from bottom to top in (b).

5-4-2. Extraction of stretch/orientation-induced reduction of "effective" friction

The multi-mode analysis of the relaxation curves adopted in Chapter 2 (procedure X[11]; *cf*. Eq. 2.4) was conducted for the $\sigma_E^-(t)/\sigma_E^-(\tau_0)$ ratio shown in Fig. 5-1 to the extract the characteristic times (τ_p) of the relaxation modes. Figure 5-2 shows plots of τ_p thus obtained against the mode number p, where p=1 corresponds to the slowest mode. When the pre-elongation is rather slow, τ_p obeys the Rouse-like scaling, $\tau_p \sim p^{-2}$ (dotted line) up to the highest mode resolved. In contrast, for fast pre-elongation, τ_p of higher modes deviate from the Rouse-like scaling and clearly indicate the acceleration effect. The acceleration factor is evaluated as the ratio of τ_p of the highest mode resolved (p = 4) to that expected from the Rouse-like scaling. The time acceleration factor thus evaluated, $\tau_p/\tau_{p,Rouse}$ with p = 4, should be affected by FENE in addition to the reduction of the "effective" friction, as similar to the experimental results described in Chapter 2. Thus, this $\tau_p/\tau_{p,Rouse}$ ratio can be expressed as $\{\zeta(F_{so})/\zeta(0)\}/f_{FENE}$, where f_{FENE} is the FENE factor accounting for the non-Gaussian behavior of the chains (*cf*. Eq. 2.6).

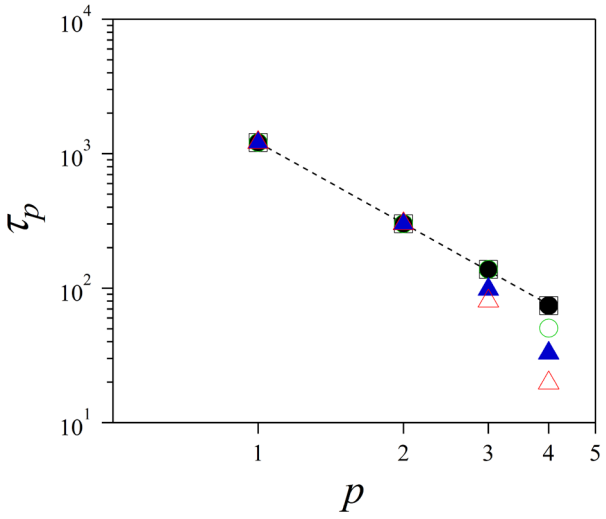

Figure 5-2 Relaxation times evaluated from the multi-exponential fit of the data in Fig. 5-1. Unfilled and filled triangles, unfilled and filled circles, and square represent the results for the stretch velocities at 0.5, 0.2, 0.1, 0.075 and 0.05 (σ/τ_0), respectively. Dotted line indicates the Rouse scaling ($\tau_p \sim p^{-2}$).

As similar to the experimental analysis (Chapter 2), the stretch/orientation factor F_{so} deduced from the KG simulation was evaluated from the stress at the cessation of the elongation. Namely, with the decoupling approximation for the internally equilibrated KG chain, the uniaxial stress at the flow cessation σ_E can be written as

$$\sigma_E = 3k_B T \nu_c f_{FENE} \lambda^2 S \tag{5.6}.$$

Here, ν_c is the number density of chains, λ is the chain stretch ratio defined with respect to the equilibrium chain size. Equation 5.6 assumes that contributions from the momentum transfer and the non-bond interactions to the stress are negligible. This assumption is reasonable at long times $t \geq \tau_0$ because the contribution from non-bond interactions relax within τ_0[9] and because the stress of the KG chain due to the momentum transfer is always much smaller than the stress due to the potential force.[12] The ratio of the extended chain length to the equilibrium end-to-end length, λ_{max} is calculated as the square root of number of Kuhn segment per chain, $\lambda_{max} = \sqrt{N_K}$ (by regarding a bead as a Kuhn segment). Then, Equation 5.6 becomes

$$\sigma_E = 3k_B T \nu_c N_K f_{FENE} \tilde{\lambda}^2 S \tag{5.7}.$$

Thus, a product of F_{so} ($= \tilde{\lambda}^2 S_p \phi_p$; *cf.* Eqs. 2.1 and 2.2) and f_{FENE} can be written as

$$F_{so} f_{FENE} = \frac{\sigma_E \phi_p}{3k_B T \nu_c N_K} \tag{5.8}.$$

For the KG simulation, the polymer volume fraction ϕ_p is a delicate parameter because of the coarse-graining nature of the simulation. For simplicity, ϕ_p in the simulation was assumed to be equivalent to a reduced volume fraction ρ/σ^3=0.85 with ρ being the bead number density, and the product $F_{so}f_{FENE}$ (Eq. 5.8) was evaluated accordingly.

In Fig. 5-3, the acceleration factor $\tau_p/\tau_{p,Rouse}$ ($= \{\zeta(F_{so})/\zeta(0)\}/f_{FENE}$) is plotted against $F_{so}f_{FENE}$ thus evaluated. The "effective" friction coefficient included in the acceleration

factor drastically reduces with increasing $F_{so}f_{FENE}$, indicating the stretch/orientation reduces of the "effective" friction even though the intrinsic friction (Γ in Eq. 5.3) is kept constant. Thus, combination of the potential forces under elongation possibly resulted in the reduction of "effective" friction in the simulation.

For comparison, the empirical result obtained in Chapter 2 (Eq. 2.8) is shown in Fig. 5-3 with the dotted curve. The KG simulation appears to give the "effective" friction reduction somewhat weaker than the experiment. This difference could be related to the *isotropic* random force acting on each bead in the simulation. This random force reduces the effective local friction even in the absence of the stretch/orientation as compared to the real polymers, and thus weakens the reduction of effective friction under fast elongation. (The entanglement, being absence in the simulation (for short chains) but present in experiments, does not appear to be the origin of this difference, because the enhancement of the orientation and stretch due to the entanglement just increases the F_{so} factor and would not significantly affect the functional form of the $\{\zeta(F_{so})/\zeta(0)\}/f_{FENE}$) factor examined in Fig. 5-3).

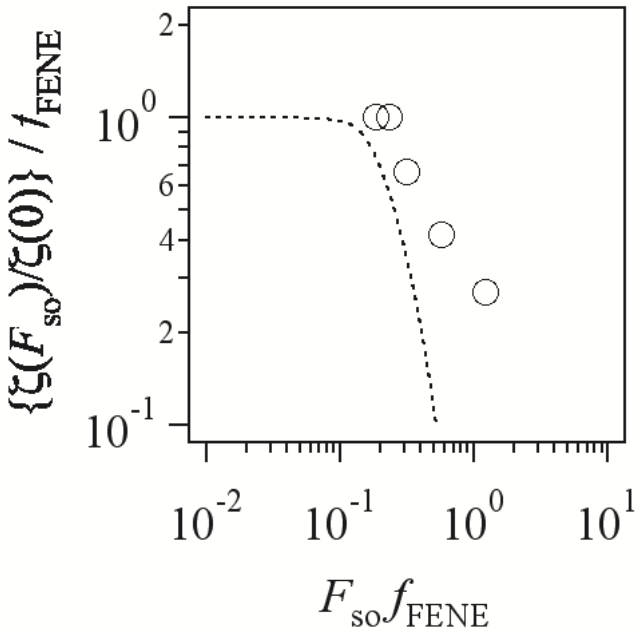

Figure 5-3 Plot of the acceleration factor $\{\zeta(F_{so})/\zeta(0)\}/f_{FENE}$) ($=\tau_p/\tau_{p,Rouse}$) against $F_{so}f_{FENE}$. Dotted curve is the empirical equation in Eq. 2.8 extracted from the data of the PS liquids.

5-5. Conclusions

The Kremer-Grest bead spring simulation was conducted to examine the stress relaxation after cessation of the uniaxial elongation. For fast pre-elongation, the relaxation was accelerated at short times but not at long times. The decrease of the characteristic time of higher relaxation modes, extracted from the simulated stress relaxation, was regarded as the reduction of the "effective" friction due to the stretch/orientation of the chain. This friction reduction from the simulations was consistent with that deduced from experimental data in literature (Chapter 2), which lends further support to the concept of stretch/orientation-induced friction reduction valid for both unentangled and entangled polymer chains.

References

1) A. Bach, K. Almdal, H. K. Rasmussen, O. Hassager, Macromolecules, 36, 5174 (2003).

2) M. H. Wagner, S. Kheirandish, O. Hassager, Journal of Rheology, 49, 1317 (2005).

3) P. K. Bhattacharjee, D. A. Nguyen, G H. McKinley, T. Sridhar, Journal of Rheology, 47, 269 (2003).

4) J. K. Nielsen, H. K. Rasmussen, O. Hassager, Journal of Rheology, 52, 885 (2008).

5) K. Kremer, G S. Grest, Journal of Chemical Physics, 92, 5057 (1990).

6) P. Mazur, I. Oppenheim, Physica (Amsterdam) 50, 241 (1970).

7) K. Kremer, G Grest, I. Carmesin, Physical Review Letters, 61, 566 (1988).

8) http://octa.jp

9) M. Kroger, M. Luap, R. Muller, Macromolecules, 30, 526 (1997).

10) M. Doi, S. F. Edwards, *"The theory of polymer dynamics"*, Oxford University Press Inc, Clarendon (1986).

11) H. Sobue, K. Murakami, Kogyo Kagaku Zasshi, 64, 2005 (1961).

12) M. Fixman, Journal of Chemical Physics, 69, 1527 (1978).

CHAPTER 6

Summary

Motivated by lack of universality observed for polymer melts and solutions under fast uniaxial elongation (Chapter 1), this thesis focused on the stretch/orientation-induced reduction of friction that could be different for melts and solutions.

In Chapter 2, the friction reduction factor was extracted from literature data of stress relaxation after cessation of fast elongational flow, and an empirical equation was formulated for this reduction.

In Chapters 3 and 4, respectively, the empirical equation for the friction reduction obtained in Chapter 2 was implemented into the multi-chain sliplink simulation and the single chain tube model. For both cases, the friction reduction due to the chain stretch/orientation led to the thinning of elongational viscosity for melts. For solutions, the simulation and tube model calculation gave thickening of elongational viscosity under fast elongational flow (because the solvent smears the orientational field.) These results strongly suggest validity of the concept of friction reduction as a factor leading to the difference between melts and solutions.

In Chapter 5, the Kremer-Grest simulations were conducted under uniaxial elongation and its cessation. The simulation kept the intrinsic segmental friction to be constant but gave acceleration of fast relaxation for highly stretched/oriented chains (possibly due to combination of the potential forces under elongation). This reduction of "effective" friction was in qualitatively agreement with the experiments (Chapter 2), suggesting the validity of the concept of stretch/orientation-induced friction reduction.

List of Publications

I. Publications included in this thesis

1. Primitive chain network simulation of elongational flows of entangled linear chains: stretch/orientation-induced reduction of monomeric friction
   Takatoshi Yaoita, Takeharu Isaki, Yuichi Masubuchi, Hiroshi Watanabe,
   Giovanni Ianniruberto, Giuseppe Marrucci
   Macromolecules, 45, 2773 (2012).
   (Chapters 2 and 3)

2. Concept of stretch/orientation-induced friction reduction tested with a simple molecular constitutive equation
   Takatoshi Yaoita, Yuichi Masubuchi, Hiroshi Watanabe
   Nihon Reoroji Gakkaishi (J. Soc. Rheol., Jpn.), 42, 207 (2014).
   (Chapter 4)

3. Stretch/orientation induced acceleration in stress relaxation in coarse-grained molecular dynamics simulations
   Yuichi Masubuchi, Takatoshi Yaoita, Yumi Matsumiya, Hiroshi Watanabe,
   Giovanni Ianniruberto, Giuseppe Marrucci
   Nihon Reoroji Gakkaishi (J. Soc. Rheol., Jpn.), 41, 35 (2013).
   (Chapter 5)

II. Other related publications

1. Highly entangled polymer primitive chain network simulations based on dynamic tube dilation

   Takatoshi Yaoita, Takeharu Isaki, Yuichi Masubuchi, Hiroshi Watanabe,

   Giovanni Ianniruberto, Francesco Greco, Giuseppe Marrucci

   Journal of Chemical Physics, 121, 12650 (2004).

2. Statics, linear, and nonlinear dynamics of entangled polystyrene melts simulated through the primitive chain network model

   Takatoshi Yaoita, Takeharu Isaki, Yuichi Masubuchi, Hiroshi Watanabe,

   Giovanni Ianniruberto, Francesco Greco, Giuseppe Marrucci

   Journal of Chemical Physics, 128, 154901 (2008).

3. Primitive chain network simulation of elongational flows of entangled linear chains: role of finite chain extensibility

   Takatoshi Yaoita, Takeharu Isaki, Yuichi Masubuchi, Hiroshi Watanabe,

   Giovanni Ianniruberto, Giuseppe Marrucci

   Macromolecules, 44, 9675 (2011).

4. Primitive chain network simulations for asymmetric star polymers

   Yuichi Masubuchi, Takatoshi Yaoita, Yumi Matsumiya, Hiroshi Watanabe

   Journal of Chemical Physics, 134, 194905 (2011).

Acknowledgements

The present thesis is based upon the study carried out under the direction of Professor Hiroshi Watanabe at Institute for Chemical Research, Kyoto University. The author would like to express the sincere gratitude to Professor Watanabe for his continuous interest and encouragement throughout this study.

The author also would like to express the sincere gratitude to Professor Yuichi Masubuchi, at Institute for Chemical Research, Kyoto University, for his constant guidance, encouragement, variable suggestions, and comments.

The author is deeply indebted to Professor Giovanni Ianniruberto and Professor Giuseppe Marrucci at Dipartimento di Ingegneria Chimica, Università degli studi di Napoli "Federico II", Professor Francesco Greco at Istituto di Ricerche sulla Combustione, CNR, Piazzale Tecchio and the members of Prof. Marrucci's group for their helpful guidance, invaluable collaborations and kind arrangements during his stay in Naples.

The author also expresses his profound gratitude to Professor Emeritus Toshiro Masuda at Department of Materials Chemistry, Kyoto University, and Dr. Takeharu Isaki at Mitsui Chemicals Inc. for providing an important opportunity to study and for their helpful advice and valuable encouragement.

Special thanks are given to Professor Hirofumi Sato at Department of Molecular Engineering, Kyoto University, and Professor Ryoichi Yamamoto at Department of Chemical Engineering, Kyoto University, for their invaluable comments.

The author is indebted to Professor Yumi Matsumiya at Institute for Chemical Research, Kyoto University, and Professor Takashi Uneyama at School of Natural System, College of Science and Engineering, Kanazawa University, for their helpful

guidance and advice.

The author acknowledges with thanks the invaluable supports and advices from Dr. Sunil Krzysztof Moorthi, Dr. Takeaki Kakigano, Dr. Yoshihiro Yamamoto, and Dr. Kunio Sannohe of Mitsui Chemicals Inc. and Mr. Jun-ichi Kakuta, Mr. Daisuke Uchida, Dr. Kyon Fun Min, Dr. Yoshitaka Matsuyama, and Dr. Kiyoshi Yamamoto of Asahi Glass Co., Ltd.

The author especially wishes to express thanks to Ms. Yukie Kajikawa, Dr. Kazushi Horio, Mr. Takeshi Suzuki, Mr. Jun Takada, Dr. Kenji Furuichi, and Dr. Hideaki Takahashi for their continuous support and encouragement throughout this study at Watanabe laboratory. The author also wishes to express thanks to all the other past and current students of Watanabe laboratory.

Finally, and most of all, the author expresses his gratitude to his wife Junko Yaoita and his sons Ryunosuke Yaoita and Jumpei Yaoita for their unwavering support and encouragement during this study. Especially, the author dedicates this thesis to his wife Junko and his sons Ryunosuke and Jumpei.

October, 2014

Takatoshi Yaoita